Nonequilibrium kinetic boundary condition at the vapor-liquid interface of argon

Tatsuya Ishiyama*
Department of Chemistry, Graduate School of Science, Tohoku University, Sendai 980-8578, Japan

Shigeo Fujikawa, Thomas Kurz, and Werner Lauterborn
Drittes Physikalisches Institut, Universität Göttingen, Friedrich-Hund-Platz 1, D-37077 Göttingen, Germany

(Received 23 August 2013; published 15 October 2013)

A boundary condition for the Boltzmann equation (kinetic boundary condition, KBC) at the vapor-liquid interface of argon is constructed with the help of molecular dynamics (MD) simulations. The KBC is examined at a constant liquid temperature of 85 K in a wide range of nonequilibrium states of vapor. The present investigation is an extension of a previous one by Ishiyama, Yano, and Fujikawa [Phys. Rev. Lett. **95**, 084504 (2005)] and provides a more complete form of the KBC. The present KBC includes a thermal accommodation coefficient in addition to evaporation and condensation coefficients, and these coefficients are determined in MD simulations uniquely. The thermal accommodation coefficient shows an anisotropic behavior at the interface for molecular velocities normal versus tangential to the interface. It is also found that the evaporation and condensation coefficients are almost constant in a fairly wide range of nonequilibrium states. The thermal accommodation coefficient of the normal velocity component is almost unity, while that of the tangential component shows a decreasing function of the density of vapor incident on the interface, indicating that the tangential velocity distribution of molecules leaving the interface into the vapor phase may deviate from the tangential parts of the Maxwell velocity distribution at the liquid temperature. A mechanism for the deviation of the KBC from the isotropic Maxwell KBC at the liquid temperature is discussed in terms of anisotropic energy relaxation at the interface. The liquid-temperature dependence of the present KBC is also discussed.

DOI: 10.1103/PhysRevE.88.042406 PACS number(s): 68.03.−g, 51.10.+y, 47.45.−n

I. INTRODUCTION

Nonequilibrium mass and energy transport phenomena across phase interfaces play crucial roles in many fields of physics, chemistry, biology, and other areas (e.g., our climate) [1–4]. Vapor-liquid interfaces are ubiquitous, and transport at the interfaces has been a focus of discussion [5], particularly in atmospheric science in heterogeneous environments such as aerosol surfaces [6] and in engineering problems as, for example, encountered in bubble dynamics [7–11]. Mass and energy transfer at a vapor-liquid interface are prescribed by the boundary condition for the Boltzmann equation (kinetic boundary condition, KBC) [12–15], and the vapor flows can be strongly influenced by the KBC [16]. There has been a long history of KBC studies since the pioneering work by Hertz [17] and Knudsen [18], and several mathematical and empirical models have been suggested based on a variety of different assumptions [7,12–14]. However, a KBC should be able to be formulated theoretically in a first-principles manner based on actual molecular interactions of the participating molecules. In this paper, we demonstrate that a KBC at a vapor-liquid interface can uniquely be constructed on a molecular interaction potential, albeit only with the help of numerical simulations. A KBC at the vapor-liquid interface of argon, which covers a fairly wide range of nonequilibrium states of vapor, is constructed based on molecular dynamics (MD) calculations of velocity distribution functions valid at the interface.

The velocity distribution function (VDF) f is defined by (see, e.g., [14])

$$dN = \frac{1}{m} f(\boldsymbol{X},\boldsymbol{\xi},t) d\boldsymbol{X} d\boldsymbol{\xi}, \tag{1}$$

where $\boldsymbol{X} = (x,y,z)$ and $\boldsymbol{\xi} = (\xi_x,\xi_y,\xi_z)$ are the molecule position with its Cartesian coordinates and the molecular velocity with its Cartesian velocity components, respectively, dN is the number of molecules in the six-dimensional volume element $d\boldsymbol{X}d\boldsymbol{\xi}$ at time t, and m is the mass of a molecule. A KBC at a vapor-liquid interface means specifying the VDF of molecules outgoing from the interface [19]. It includes information on the number and the velocities of molecules emitted from the interface. From mass, momentum, and energy conservation, all transport of molecules across the interface is prescribed by the KBC. A KBC also includes which fraction of molecules incident on the interface condenses onto the interface. The "condensation coefficient" or the "mass accommodation coefficient" α_c has been widely used as the parameter to specify the condensation probability, and it has long been studied experimentally [20–22] and theoretically [23,24].

The MD simulation is a quite useful tool to resolve heat and mass transfer at the interface from a molecular point of view, and details of the molecular condensation mechanism have been reported [25–34]. The evaporation from a liquid is also relevant for the mass transfer at a vapor-liquid interface [35,36], and the "evaporation coefficient" α_e as well as the condensation coefficient has been a matter of debate [37–42]. However, energy transfer is not determined uniquely only by the condensation-evaporation ratio. The "thermal accommodation coefficient" α_t is frequently used to specify

*ishiyama@m.tohoku.ac.jp

to what extent the molecules reflected to the vapor phase are thermally accommodated to the liquid temperature [14]. In most studies, the parameters α_c, α_e, and α_t have been examined separately. However, as we shall demonstrate, those coefficients and corresponding VDFs should not be examined separately, because mass and energy transfer is uniquely given in the framework of VDFs (i.e., KBCs). In this paper, we derive the KBC containing α_c, α_e, and α_t and determine their values for a real monoatomic molecule.

The present KBC study is based on a series of previous results [37,43], and an extension of a previous letter [44], where the modeling of energy transfer had not yet been completed. The present investigation provides a more complete form of the boundary condition including α_t. We also discuss molecular mechanisms leading to the KBC constructed in this study. Section II describes the outline of the KBC construction. Readers may find an essential part pertaining to the present context and results in Sec. II without consulting the previous publications and other sections in detail. In Sec. III, details of the present MD procedures are summarized. Section IV is devoted to the calculation results of the VDF of molecules leaving the interface and of the three coefficients α_c, α_e, and α_t. Some additional analyses to clarify the physical origin of the KBC form derived are presented there together with a discussion of the temperature dependence of the new KBC. Concluding remarks follow in Sec V.

II. FORMULATION OF THE KINETIC BOUNDARY CONDITION AT A VAPOR-LIQUID INTERFACE

Here we outline the present formulation of the KBC and the results of MD simulations to be discussed in detail in the subsequent sections. As shown in Fig. 1, vapor molecules colliding with a plane vapor-liquid interface and molecules outgoing from the interface thereby crossing a transition layer are considered. The VDFs of those molecules are defined as $f^{\rm coll}$ and $f^{\rm out}$, respectively. The mass fluxes of those molecules are then determined without any assumptions as

$$\langle J^{\rm coll}\rangle = -\int_{\xi_z<0} \xi_z f^{\rm coll} d\boldsymbol{\xi}, \tag{2a}$$

$$\langle J^{\rm out}\rangle = \int_{\xi_z>0} \xi_z f^{\rm out} d\boldsymbol{\xi}, \tag{2b}$$

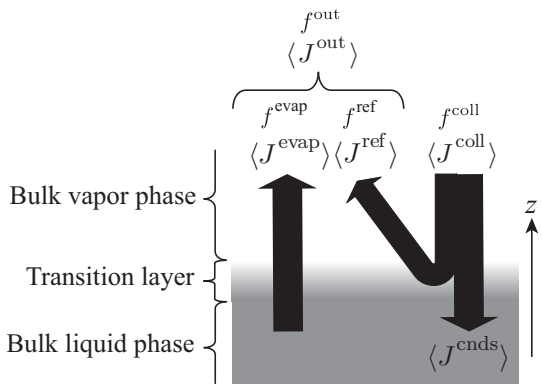

FIG. 1. Definitions of velocity distribution functions f and molecular fluxes J at a vapor-liquid interface.

where ξ_z is the molecular velocity component normal to the interface, and the positive z direction is defined as the direction from liquid to vapor. Hereafter, we denote the three-dimensional integral $\int_{-\infty}^{\infty}\int_{-\infty}^{\infty}\int_{-\infty}^{\infty} d\xi_x d\xi_y d\xi_z$ as $\int d\boldsymbol{\xi}$ and the three-dimensional half-space integral $\int_0^{\infty}\int_{-\infty}^{\infty}\int_{-\infty}^{\infty} d\xi_x d\xi_y d\xi_z$ as $\int_{\xi_z>0} d\boldsymbol{\xi}$, and so on. In the equilibrium state at temperature T, $f^{\rm coll}(-\xi_z) = f^{\rm out}(\xi_z) = \rho_v(T)\hat{f}^*(T)$ (for $\xi_z > 0$) holds, where $\rho_v(T)$ is the saturated vapor density at temperature T, and $\hat{f}^*(T)$ denotes the normalized Maxwell VDF at temperature T,

$$\hat{f}^*(T) = \hat{f}_x^*(T)\hat{f}_y^*(T)\hat{f}_z^*(T), \tag{3}$$

where $\hat{f}_\iota^*(T)$ is the one-dimensional, normalized Gaussian distribution function of the molecular velocity with a temperature T of the ιth direction ($\iota = x,y,z$), T_ι, here also called component VDF:

$$\hat{f}_\iota^*(T_\iota) = \frac{1}{\sqrt{2\pi RT_\iota}} \exp\left(-\frac{\xi_\iota^2}{2RT_\iota}\right), \tag{4}$$

where $R = k_B/m$ is the gas constant with $k_B(= 1.380\,65 \times 10^{-23}$ J/K) being the Boltzmann constant. It may be considered as one component of the Maxwell VDF. In the above expressions, $*$ represents a Gaussian distribution, and $\hat{}$ represents a function normalized in the whole molecular velocity space.

$f^{\rm coll}$ is usually obtained as a solution of the Boltzmann equation, while $f^{\rm out}$ (i.e., the KBC) is unknown at the level of kinetic theory and should be modeled in MD calculations. Intuitively, $f^{\rm out}$ should depend on both gas and liquid states. Here, we assume that $f^{\rm out}$ is a function of $f^{\rm coll}$ and liquid temperature T_ℓ, as well as molecular velocity $\boldsymbol{\xi}$: $f^{\rm out}(f^{\rm coll}, T_\ell, \boldsymbol{\xi})$. The problem is how to model $f^{\rm out}$ as a function of $f^{\rm coll}$ at a fixed T_ℓ. The temperature dependence of $f^{\rm out}$ will be discussed in the next step (Sec. IV G).

The KBC approach by Ishiyama *et al.* divides $f^{\rm out}$ into the following two parts [37]:

$$\begin{aligned} f^{\rm out}(f^{\rm coll}, T_\ell, \boldsymbol{\xi}) &= f^{\rm out}(0, T_\ell, \boldsymbol{\xi}) \\ &\quad + [f^{\rm out}(f^{\rm coll}, T_\ell, \boldsymbol{\xi}) - f^{\rm out}(0, T_\ell, \boldsymbol{\xi})] \\ &= f^{\rm evap}(0, T_\ell, \boldsymbol{\xi}) + f^{\rm ref}(f^{\rm coll}, T_\ell, \boldsymbol{\xi}). \end{aligned} \tag{5}$$

Here, we call the first term on the right-hand side of Eq. (5) the VDF of molecules evaporating from the interface spontaneously, since it is independent of $f^{\rm coll}$.

$f^{\rm evap}$ can uniquely be determined in vacuum evaporation MD simulations [37,43], and then the mass flux of evaporating molecules is obtained as

$$\langle J^{\rm evap}\rangle = \int_{\xi_z>0} \xi_z f^{\rm evap} d\boldsymbol{\xi}. \tag{6}$$

There may be other, different ways to split $f^{\rm out}$, if $f^{\rm out}$ is well modeled in some range of nonequilibrium states [26,33,45–47]. Actually, some studies employed another way to split $f^{\rm out}$ into two VDFs by labeling an outgoing molecule as an evaporated or a reflected one [26,33,45]. We emphasize here that the splitting of $f^{\rm out}$ in Eq. (5) is free from such a distinction of individual molecules.

Next, some mass fluxes at the vapor-liquid interface are defined, as schematically shown in Fig. 1: $\langle J^{\rm coll}\rangle$,

$\langle J^{\rm out}\rangle$, and $\langle J^{\rm evap}\rangle$ are defined above, and $\langle J^{\rm ref}\rangle$ is the mass flux of molecules reflected at the interface, defined as $\langle J^{\rm out}\rangle - \langle J^{\rm evap}\rangle$, and then $\langle J^{\rm cnds}\rangle$ is that of molecules condensing onto the interface, defined as $\langle J^{\rm coll}\rangle - \langle J^{\rm ref}\rangle$:

$$\langle J^{\rm ref}\rangle = \langle J^{\rm out}\rangle - \langle J^{\rm evap}\rangle, \tag{7a}$$

$$\langle J^{\rm cnds}\rangle = \langle J^{\rm coll}\rangle - \langle J^{\rm ref}\rangle. \tag{7b}$$

All the VDFs and mass fluxes introduced can be determined without any ambiguity in MD simulations. The condensation coefficient α_c and the evaporation coefficient α_e are defined as

$$\alpha_c = \frac{\langle J^{\rm cnds}\rangle}{\langle J^{\rm coll}\rangle}, \tag{8a}$$

$$\alpha_e = \frac{\langle J^{\rm evap}\rangle}{\langle J^{\rm out}\rangle_{\rm e}} = \frac{\langle J^{\rm evap}\rangle}{\rho_v(T_\ell)\sqrt{RT_\ell/(2\pi)}}, \tag{8b}$$

where $\langle J^{\rm out}\rangle_{\rm e}$ is the outgoing mass flux in the equilibrium state. In the equilibrium state, $\alpha_c = \alpha_e$ holds, since $\langle J^{\rm coll}\rangle = \rho_v(T_\ell)\sqrt{RT_\ell/(2\pi)}$ and $\langle J^{\rm cnds}\rangle = \langle J^{\rm evap}\rangle$, while these relations are not necessarily guaranteed in nonequilibrium states.

In Sec. IV C, α_c will be examined at a constant liquid temperature of 85 K of argon in a wide range of nonequilibrium states of its vapor. In previous reports [37,44] it has been demonstrated that $f^{\rm evap}$ and $f^{\rm out}$, obtained from the MD simulations, can be expressed in the following functional forms:

$$f^{\rm evap} = \sigma^{\rm evap}\hat{f}_x^*(T_\ell)\hat{f}_y^*(T_\ell)\hat{f}_z^*(T_\ell) \quad (\xi_z > 0), \tag{9}$$

$$f^{\rm out} = \sigma^{\rm out}\hat{f}_x^*(T_t)\hat{f}_y^*(T_t)\hat{f}_z^*(T_\ell) \quad (\xi_z > 0), \tag{10}$$

where $\sigma^{\rm evap}$ and $\sigma^{\rm out}$ will be determined by the mass flux relations, Eqs. (7a) and (7b), as described subsequently, and T_t will be defined and related to other quantities further below. Substituting Eq. (9) into Eq. (6), we have $\langle J^{\rm evap}\rangle = \sigma^{\rm evap}\sqrt{RT_\ell/(2\pi)}$, and from the definition of α_e [Eq. (8b)],

$$\sigma^{\rm evap} = \alpha_e\rho_v. \tag{11}$$

Thus $f^{\rm evap}$ can be expressed as

$$f^{\rm evap} = \alpha_e\rho_v(T_\ell)\hat{f}_x^*(T_\ell)\hat{f}_y^*(T_\ell)\hat{f}_z^*(T_\ell) \quad (\xi_z > 0). \tag{12}$$

Similarly, substituting Eq. (10) into Eq. (2b), we have $\langle J^{\rm out}\rangle = \sigma^{\rm out}\sqrt{RT_\ell/(2\pi)} = \langle J^{\rm evap}\rangle + \langle J^{\rm ref}\rangle = \langle J^{\rm evap}\rangle + \langle J^{\rm coll}\rangle(1 - \langle J^{\rm cnds}\rangle/\langle J^{\rm coll}\rangle)$, where the mass flux relationships of Eqs. (7) are applied. Thus we obtain [44]

$$\sigma^{\rm out} = \alpha_e\rho_v + (1-\alpha_c)\langle J^{\rm coll}\rangle/\sqrt{RT_\ell/(2\pi)}, \tag{13}$$

$$f^{\rm out} = [\alpha_e\rho_v + (1-\alpha_c)\sigma_w]\hat{f}_x^*(T_t)\hat{f}_y^*(T_t)\hat{f}_z^*(T_\ell) \quad (\xi_z > 0), \tag{14}$$

where $\sigma_w = \langle J^{\rm coll}\rangle/\sqrt{RT_\ell/(2\pi)}$. Equation (14) is the physically correct KBC which we have sought, but the parameter T_t in Eq. (14) is still unknown as a function of $f^{\rm coll}$ and the next step is to express T_t in a suitable form.

A component temperature of a VDF f is defined as [7,12–14]

$$T_\iota = \frac{1}{\rho R}\int(\xi_\iota - v_\iota)^2 f\,d\boldsymbol{\xi} \quad (\iota = x \text{ or } y \text{ or } z), \tag{15}$$

where the density ρ and the velocity v_ι are defined as

$$\rho = \int f\,d\boldsymbol{\xi}, \tag{16}$$

$$v_\iota = \frac{1}{\rho}\int \xi_\iota f\,d\boldsymbol{\xi}. \tag{17}$$

According to these definitions, a component temperature of the outgoing molecules, $T_\iota^{\rm out}$ ($\iota = x$ or y or z), is defined by

$$T_\iota^{\rm out} = \frac{1}{\rho^{\rm out}R}\int_{\xi_z>0}\left(\xi_\iota - v_\iota^{\rm out}\right)^2 f^{\rm out}d\boldsymbol{\xi}, \tag{18}$$

where

$$\rho^{\rm out} = \int_{\xi_z>0} f^{\rm out}d\boldsymbol{\xi}, \tag{19}$$

$$v_\iota^{\rm out} = \frac{1}{\rho^{\rm out}}\int_{\xi_z>0}\xi_\iota f^{\rm out}d\boldsymbol{\xi}. \tag{20}$$

Substituting Eq. (10) into Eqs. (18), (19), and (20), we obtain $\rho^{\rm out} = \sigma^{\rm out}/2$, $v_\iota^{\rm out} = 0$ for $\iota = x$ or y, $v_z^{\rm out} = \sqrt{2RT_\ell/\pi}$,

$$T_\iota^{\rm out} \equiv T_t, \quad \text{for} \quad \iota = x \text{ or } y, \tag{21}$$

and $T_z^{\rm out} = (1 - 2/\pi)T_\ell$.

It will be shown in Sec. IV B (compare Ref. [44]) that $T_\iota^{\rm out}(= T_t)$ for $\iota = x$ or y may largely deviate from T_ℓ depending on the states of vapor. We discuss the mechanism why T_t deviates from T_ℓ in terms of anisotropic energy relaxation at the interface in Sec. IV E.

The tangential temperature T_t is given by $f^{\rm out}$ in Eq. (18), but, in principle, it should be a function of the VDF of the incident, colliding molecules, $f^{\rm coll}$. In Ref. [44], T_t was given as a linear function of the incident energy flux, $E^{\rm coll}$. In this paper, we develop a more advanced expression for T_t to give the KBC a more tractable form in an actual application.

In the following, T_t is formulated as a function of $f^{\rm coll}$ by introducing the thermal accommodation coefficient α_t (see below). From Eqs. (5), (12), and (14) $f^{\rm ref}$ can be formulated as

$$f^{\rm ref} = f^{\rm out} - f^{\rm evap} \tag{22a}$$

$$= \{[\alpha_e\rho_v + (1-\alpha_c)\sigma_w]\hat{f}_x^*(T_t)\hat{f}_y^*(T_t) - \alpha_e\rho_v\hat{f}_x^*(T_\ell)\hat{f}_y^*(T_\ell)\}\hat{f}_z^*(T_\ell) \quad (\xi_z > 0) \tag{22b}$$

$$\equiv \sigma^{\rm ref}\hat{f}_x^{\rm ref}\hat{f}_y^{\rm ref}\hat{f}_z^*(T_\ell) \quad (\xi_z > 0), \tag{22c}$$

where $\hat{f}_\iota^{\rm ref}$ ($\iota = x$ or y) is the normalized VDF of the reflected component tangential to the interface and is not necessarily a Gaussian distribution. Similar to the case of $T_\iota^{\rm out}$, defined in Eq. (18), a component temperature of the reflection is defined as

$$T_\iota^{\rm ref} = \frac{1}{\rho^{\rm ref}R}\int_{\xi_z>0}\left(\xi_\iota - v_\iota^{\rm ref}\right)^2 f^{\rm ref}d\boldsymbol{\xi} \quad (\iota = x \text{ or } y \text{ or } z), \tag{23}$$

where

$$\rho^{\rm ref} = \int_{\xi_z>0} f^{\rm ref}d\boldsymbol{\xi}, \tag{24}$$

$$v_\iota^{\rm ref} = \frac{1}{\rho^{\rm ref}}\int_{\xi_z>0}\xi_\iota f^{\rm ref}d\boldsymbol{\xi}. \tag{25}$$

Substituting Eq. (22b) into Eqs. (23), (24), and (25), we obtain $\rho^{\rm ref} = \sigma^{\rm ref}/2$, $v_\iota^{\rm ref} = 0$ for $\iota = x$ or y, $v_z^{\rm ref} = \sqrt{2RT_\ell/\pi}$, and $T_z^{\rm ref} = (1-2/\pi)T_\ell$. $\sigma^{\rm ref}$ in Eq. (22c) can be evaluated by taking the integral $\int f^{\rm ref} d\boldsymbol{\xi}$ for Eqs. (22b) and (22c) to get

$$\sigma^{\rm ref} = (1-\alpha_c)\sigma_w, \tag{26}$$

and $T_\iota^{\rm ref} \equiv T_r$ for $\iota = x$ or y can be written as $T_r = T_t + (T_t - T_\ell)\alpha_e\rho_v/[(1-\alpha_c)\sigma_w]$, or, rearranged for T_t,

$$T_t = \frac{\alpha_e\rho_v T_\ell + (1-\alpha_c)\sigma_w T_r}{\alpha_e\rho_v + (1-\alpha_c)\sigma_w}. \tag{27}$$

For $T_r = T_\ell$, the tangential temperature T_t of a mixture consisting of spontaneously evaporating and of reflected components becomes T_ℓ, as it should be.

Equation (27) expresses the relationship between T_t and T_r. The remaining problem is how to model T_r as a function of $f^{\rm coll}$. To do this, we introduce the thermal accommodation coefficient α_t defined through

$$T_r = \alpha_t T_\ell + (1-\alpha_t)T_c, \tag{28}$$

where $T_c \equiv T_\iota^{\rm coll}$ ($\iota = x$ or y) is the tangential temperature of incident, colliding molecules:

$$T_\iota^{\rm coll} = \frac{1}{\rho^{\rm coll}R}\int_{\xi_z<0} \xi_\iota^2 f^{\rm coll} d\boldsymbol{\xi} \quad (\iota = x \text{ or } y), \tag{29}$$

in which

$$\rho^{\rm coll} = \int_{\xi_z<0} f^{\rm coll} d\boldsymbol{\xi} = \sigma^{\rm coll}/2, \tag{30}$$

because $f^{\rm coll} = \sigma^{\rm coll}\hat{f}^{\rm coll}$. In Eq. (29), we assume that $f^{\rm coll}$ has symmetry in x and y directions, i.e., $v_\iota^{\rm coll} = \int_{\xi_z<0} \xi_\iota f^{\rm coll} d\boldsymbol{\xi}/\rho^{\rm coll} = 0$ for $\iota = x$ and y. We finally obtain $f^{\rm out}$ as a function of $f^{\rm coll}$ via the three parameters α_e,α_c, and α_t.

Equation (28) provides us with a physical picture that the temperature of the reflected molecules can be viewed as an intermediate state between complete accommodation (the first term with $\alpha_t = 1$) and no accommodation at all (the second term with $\alpha_t = 0$). In this sense, the functional form that Eq. (22c) contains $\hat{f}_z^*(T_\ell)$ implies that the normal (perpendicular) temperature of outgoing molecules is completely accommodated (i.e., $\alpha_t = 1$ in the z direction). In Sec. IV D, we will actually calculate the value of α_t for argon in MD simulations and model α_t as a function of the states of vapor. The mechanism of the anisotropic behavior of α_t is discussed in Sec. IV E. Once α_t is modeled, T_t can be determined as a function of $f^{\rm coll}$ from Eqs. (27), (28), and (29), and hence the correct KBC $f^{\rm out}$, Eq. (14), is given as a function of $f^{\rm coll}$ explicitly with the help of the coefficients α_e, α_c, α_t. Heat and mass transfer at the interface can be described by those coefficients. Note that the correct KBC should show $T_t \to T_\ell$ in the cases of vacuum evaporation ($f^{\rm coll} = 0$) and equilibrium state [$f^{\rm coll} = \rho_v \hat{f}_x^*(T_\ell)\hat{f}_y^*(T_\ell)\hat{f}_z^*(T_\ell)$]. One can easily check that these necessary conditions are automatically satisfied in the above formulations.

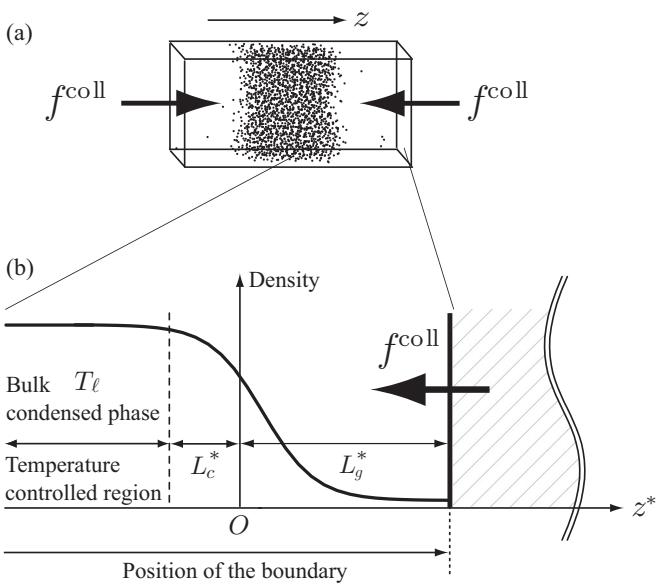

FIG. 2. (a) The molecular dynamics system. (b) Schematic of the control variables in the moving coordinate system z^*.

III. MOLECULAR DYNAMICS PROCEDURES

The MD procedures are essentially the same as the ones in a previous report [44]. Here, we give a more detailed description of the computation. The phenomenon considered here is the one-dimensional steady evaporation or condensation flow in the macroscopic sense. To construct such a nonequilibrium system, we prepare a rectangular MD simulation cell containing a liquid slab and its vapor [Fig. 2(a)]. The two vapor-liquid interfaces are formed in the (x,y) plane. The lateral dimensions are set to $L_x \times L_y = 50 \times 50$ Å^2, and the initial length L_z is 88.3 Å, which is changed in the course of calculation as explained later. Initially, the simulation cell imposing three-dimensional periodic boundary conditions contains 2000 argon molecules in a vapor-liquid equilibrium state at 85 K, forming a liquid slab with thickness ~38.2 Å at the center of the cell. The 12-6 Lennard-Jones potential $\phi(r_{ij}) = 4\epsilon[(\sigma/r_{ij})^{12} - (\sigma/r_{ij})^6]$ is applied for the intermolecular potential of argon molecules with a cutoff length of 15 Å, where $\sigma = 3.405$ Å, $\epsilon/k_B = 119.8$ K, and r_{ij} is the intermolecular distance between the ith and jth molecules. Newton's equations of motion are integrated numerically using the leapfrog algorithm with a time step of 1 fs.

After the equilibration during several hundreds of picoseconds, the boundary condition in the z direction (normal to the interface) is changed in the following way to construct the nonequilibrium steady evaporation and condensation states. Note that the periodic boundary condition is kept in the x and y directions. At the boundaries of the simulation cell faces in the $\pm z$ direction (hereafter referred to as the top and bottom faces, respectively) we utilize an algorithm widely used in the direct simulation Monte Carlo method [48]. That is, we give the positions and velocities of molecules colliding with the interface across the top or bottom face probabilistically with the help of uniformly distributed random numbers R_n ($0 \leqslant R_n \leqslant 1$), and we eliminate the molecules exiting across these boundaries. The position of the ith molecule entering

the cell is determined as $(x^i, y^i) = (L_x R_1, L_y R_2)$ in the top or bottom face. To avoid unphysical overlap of intermolecular potentials, the position (x^i, y^i) is rejected if $r_{ij} < \sigma$ for some jth molecule, and the random numbers are regenerated until $r_{ij} > \sigma$ is satisfied for any other jth molecule. The velocities of molecules penetrating the interface are given, according to the direct method [48], on the basis of a specified distribution function $f^{\rm coll}$, for which we assume the Maxwell-type distribution function,

$$f^{\rm coll} = \beta\rho_v \hat{f}_x^*(\gamma T_\ell)\hat{f}_y^*(\gamma T_\ell)\hat{f}_z^*(\gamma T_\ell), \tag{31}$$

for $\xi_z < 0$ on the top face and for $\xi_z > 0$ on the bottom one. In the direct method, the velocity of the ith molecule according to $f^{\rm coll}$ in Eq. (31) is determined as

$$\xi_x^i = \sqrt{-2\gamma RT_\ell \ln(R_1)}\cos 2\pi R_2,$$
$$\xi_y^i = \sqrt{-2\gamma RT_\ell \ln(R_1)}\sin 2\pi R_2,$$
$$\xi_z^i = \sqrt{-2\gamma RT_\ell \ln(R_3)}.$$

Here, β and γ are parameters that represent the deviation from the equilibrium state. The factors β and γ can be considered as describing, respectively, a deviation from the saturation vapor density ρ_v ($\rho_v \to \beta\rho_v$) and a vapor temperature deviation from the liquid temperature T_ℓ ($T_\ell \to \gamma T_\ell$). The equilibrium state corresponds to $\beta = \gamma = 1$, and the vacuum evaporation state [37] is realized when $\beta = 0$. We present the results of numerical simulations for 20 different sets of $\beta = 0.5$, 1.0, 2.0, 3.0, and 4.0 and $\gamma = 1.0$, 2.0, 3.0, and 4.0. As shown later, the net condensation occurs in the parameter sets of $\beta > 1.0$ and $\gamma > 1.0$, since the temperature and pressure in the vapor phase become higher compared with those in the equilibrium state. On the other hand, the simulations with $\beta = 0.5$ create systems with net evaporation in the range of $\gamma < 4.0$. Note that the compression factor $p/(\rho RT)$ is confirmed to be nearly unity in all cases, and hence the vapor can be regarded as an ideal gas.

From now, we focus on the dynamics of molecules in the right-half region in the cell [Fig. 2(a)] because the vapor-liquid system is symmetric with respect to the center of the liquid layer in the macroscopic sense. The thickness of the liquid slab increases with time when net condensation occurs, whereas it decreases when net evaporation occurs. In the former (latter) case, the interface moves toward the vapor (liquid) phase. We therefore introduce the moving coordinate system z^*, as shown in Fig. 2(b), where

$$z^* = \frac{z - (Z_m - v_s t)}{\delta}, \tag{32a}$$

$$v_s = \frac{J_s}{\rho_\ell}, \tag{32b}$$

where Z_m and δ are, respectively, the center position (the so-called Gibbs dividing surface position [49]) and the 10–90 thickness of the transition layer (6.3 Å at 85 K for argon), which have already been obtained in the equilibrium simulation [37], v_s is the speed of the moving coordinate, t is the time from the beginning of the simulation, ρ_ℓ is the liquid density, and J_s is the nonaveraged net mass flux across the top face. To realize a steady condensation state, the distance between the top face and Z_m, L_g^* in Fig. 2(b), should be unchanged during the simulation. The cell length L_z is therefore changed so as to maintain this distance. The liquid slab is thermostatted at T_ℓ with the velocity scaling method [50] for the region of $z^* < -L_c^*$ in Fig. 2(b). We checked that the present results are insensitive in the range of $2 < L_g^* < 4$ and $0 < L_c^* < 1$, and we employed $L_g^* = 4$ and $L_c^* = 1$. After a steady state is established, samples are accumulated throughout the simulation time of several tens of nanoseconds, and statistical averages are calculated on the z^* coordinate from tens of millions of samples.

IV. RESULTS AND DISCUSSION

A. Density, velocity, and temperature near the interface

In Fig. 3, density, velocity, and temperature profiles calculated by MD simulations for various (β,γ) sets are shown versus the moving coordinate z^*. In the case of $\beta = \gamma = 1.0$ (crosses), one can confirm that the vapor-liquid equilibrium is realized (i.e., $\rho = \rho_v$, $v = 0$, and $T = T_\ell$). For $\beta = \gamma = 2.0$ (filled circles) and 4.0 (solid squares), the vapor has a higher density than ρ_v and negative velocities of the molecules, which means a net condensation state. In the case of $\beta = 0.5, \gamma = 1.0$ (open circles), on the other hand, net evaporation occurs. One can also see that the profiles are almost constant in the region of $2 < z^* < 4$ of width 2δ compared to the transition region ($0 < z^* < 2$). This suggests that molecular collisions among vapor molecules rarely occur and/or attractive interaction from the liquid is negligible in the region $2 < z^* < 4$. Since the Knudsen numbers [=mean free path/(2δ)] in the region $2 < z^* < 4$ are large compared to unity for the present nonequilibrium vapor [44], the kinetic interface may be located at an arbitrary z^* position in the range $2 < z^* < 4$. We therefore evaluate $f^{\rm out}$ by sampling the molecular velocity in the region $2 < z^* < 4$.

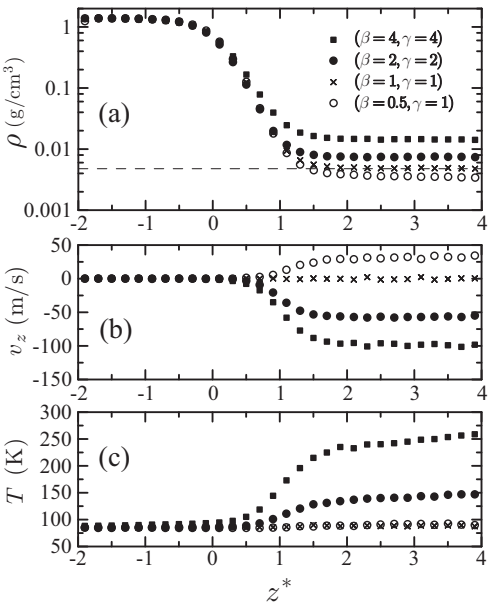

FIG. 3. Density, velocity, and temperature distributions for some cases of (β,γ). The dashed line in (a) denotes the saturated vapor density ρ_v for $T_\ell = 85$ K: $\rho_v = 4.59 \times 10^{-3}$ g/cm^3.

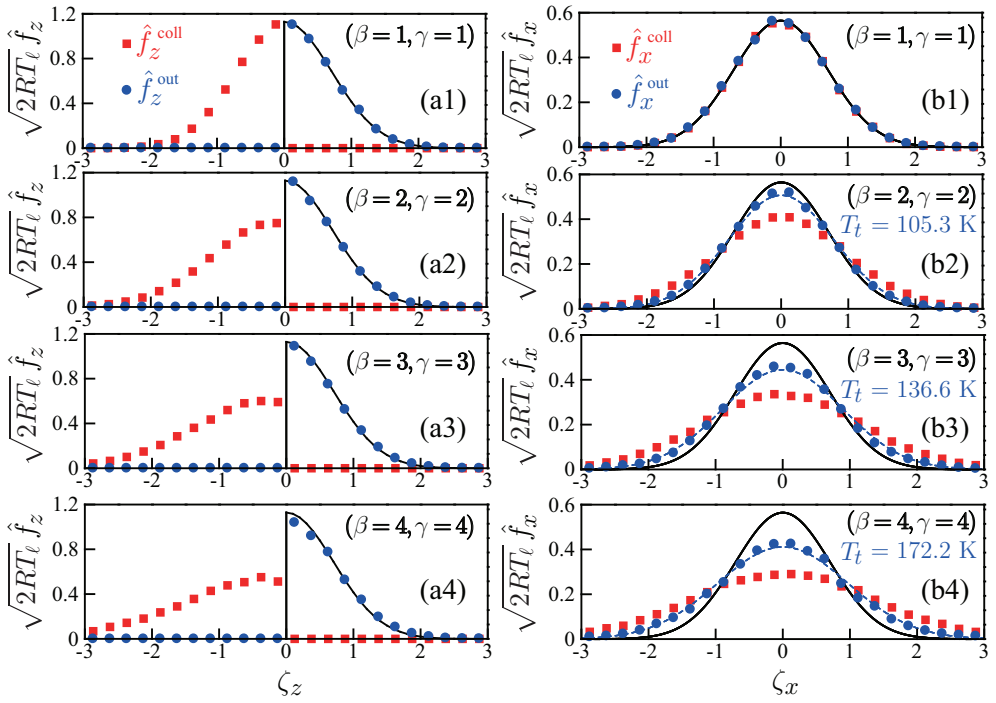

FIG. 4. (Color online) Normalized velocity distribution function of molecules incident onto the interface, $\hat{f}^{\rm coll}$ (red squares), and outgoing from the interface, $\hat{f}^{\rm out}$ (blue circles), calculated in MD simulations at $T_\ell = 85$ K, where $\zeta_\iota = \xi_\iota/\sqrt{2RT_\ell}$ ($\iota = x,z$). The solid curves in the left panels denote one-dimensional, normalized reduced half-Maxwell velocity distributions with T_ℓ (= 85 K): $(2/\sqrt{\pi})\,\exp(-\zeta_z^2)$ ($\zeta_z > 0$); those in the right panels denote one-dimensional, normalized reduced Maxwell velocity distributions with T_ℓ: $(1/\sqrt{\pi})\,\exp(-\zeta_x^2)$. The dotted curves in the right panels are one-dimensional, normalized reduced Maxwell velocity distributions with different temperatures T_t: $\sqrt{T_\ell/(T_t\pi)}\,\exp(-\zeta_x^2 T_\ell/T_t)$.

B. Functional form of $f^{\rm out}$ in nonequilibrium states

VDFs of molecules outgoing from the interface into the vapor, $f^{\rm out}$, are examined by sampling the molecular velocity with $\xi_z > 0$ in the region $2 < z^* < 4$ under various $f^{\rm coll}$ determined by Eq. (31). Figure 4 shows some representative results for $f^{\rm coll}$ with the parameter sets (β,γ) = (1,1), (2,2), (3,3), and (4,4). In the upper panels in Fig 4, the normalized VDFs in the case of $\beta = \gamma = 1.0$ (i.e., the equilibrium state) are shown, where Figs. 4(a1) and 4(b1) show the VDFs normal and tangential to the interface, respectively. The red squares denote $\hat{f}^{\rm coll}$ and the blue circles denote $\hat{f}^{\rm out}$. One can clearly see that the equilibrium state is realized in the case of $\beta = \gamma = 1$. Now we focus on the left panels of Fig. 4. $\hat{f}_z^{\rm coll}$ has a wider distribution from upper (a1) to lower (a4) panels, since the input parameter γ increases. Nevertheless, the response $\hat{f}_z^{\rm out}$ shows the (half) component Maxwell VDF at T_ℓ. Interestingly, the situation is different in the case of the tangential components, as shown in the panels of Fig. 3. One can clearly recognize that the response $\hat{f}_x^{\rm out}$ shows the component Maxwell VDF with the temperature T_t, and T_t is in the range between the liquid temperature T_ℓ and the temperature of the input vapor (γT_ℓ). In Table I, T_t values calculated in MD simulations by Eq. (18) are listed.

Accordingly, the functional form of $f^{\rm out}$ shown in Eq. (10) is demonstrated. The result suggests that the normal velocity component is completely accommodated at T_ℓ, while the tangential velocity component shows incomplete accommodation. In Sec. IV D, we will show the thermal accommodation coefficient for the present parameter sets (β,γ) calculated in MD simulations and discuss the mechanism of the anisotropic accommodation in Sec. IV E.

C. Evaporation and condensation coefficients

Here, we evaluate the condensation coefficient α_c in nonequilibrium MD simulations via Eq. (8a). The evaporation coefficient has already been reported for argon at 85 K as $\alpha_e \sim 0.868$ [37], which is equal to the condensation coefficient in the equilibrium state by definition. In MD simulations, $\langle J^{\rm out}\rangle$ and $\langle J^{\rm coll}\rangle$ can easily be evaluated by counting the number of molecules per unit area and per unit time leaving ($\langle J^{\rm out}\rangle$) or entering ($\langle J^{\rm coll}\rangle$) the simulation boundary [see Fig. 2(b)]. $\langle J^{\rm out}\rangle$ and $\langle J^{\rm coll}\rangle$ values are listed in Table I. $\langle J^{\rm evap}\rangle$ has already been obtained in vacuum evaporation simulations [37]. The mass fluxes $\langle J^{\rm ref}\rangle$ and $\langle J^{\rm cnds}\rangle$ are determined by Eqs. (7). The calculated condensation coefficients obtained from Eq. (8a) are shown as a function of β and γ in Fig. 5 and in Table I. In the range of net condensation states ($\beta > 1.0$ and $\gamma > 1.0$), α_c is almost constant and equal to α_e. In the net evaporation regime ($\beta = 0.5$), α_c seems to be slightly lower than α_e. An accurate evaluation of α_c for the net evaporation regime may be more difficult to obtain than that for the net condensation regime, since $\langle J^{\rm coll}\rangle$ in the denominator of Eq. (8a) is small, and the value of α_c may be sensitive to the value of $\langle J^{\rm evap}\rangle$. Nevertheless, $\alpha_c \approx \alpha_e$ is a good approximation near the equilibrium state; such a relation between α_c and α_e is confirmed by experiments for water and methanol (see Fig. 3.24 of [7]).

TABLE I. The results of the nonequilibrium simulations of argon at 85 K.

β	γ	$\langle J^{\rm coll}\rangle$ [g/(cm^2 s)]	$\langle J^{\rm out}\rangle$ [g/(cm^2 s)]	α_c	T_t (K)	T_c (K)	α_t
0.5	1.0	12.71	23.94	0.834	83.12	86.26	—
1.0	1.0	25.39	24.51	0.894	85.06	85.08	—
2.0	1.0	51.08	26.48	0.909	88.67	87.73	—
3.0	1.0	76.18	29.05	0.905	85.81	85.28	—
4.0	1.0	102.22	32.38	0.897	88.47	85.66	—
0.5	2.0	17.70	24.22	0.865	88.26	158.85	0.947
1.0	2.0	36.10	25.79	0.89	98.70	165.31	0.810
2.0	2.0	71.74	28.66	0.905	105.35	162.77	0.721
3.0	2.0	106.79	31.51	0.909	112.34	162.72	0.632
4.0	2.0	144.19	38.35	0.885	115.70	162.68	0.594
0.5	3.0	21.74	24.81	0.863	92.76	231.04	0.939
1.0	3.0	43.81	26.26	0.899	104.03	235.18	0.860
2.0	3.0	87.91	31.8	0.887	125.19	242.94	0.734
3.0	3.0	130.82	36.27	0.89	136.64	243.00	0.663
4.0	3.0	173.72	46.05	0.861	146.71	252.66	0.625
0.5	4.0	25.64	25.67	0.85	100.91	316.54	0.923
1.0	4.0	50.57	27.95	0.879	119.40	310.72	0.836
2.0	4.0	101.77	36.3	0.858	143.46	314.93	0.738
3.0	4.0	148.70	41.69	0.866	157.02	321.68	0.689
4.0	4.0	203.11	50.14	0.861	172.18	318.11	0.620

D. Thermal accommodation coefficient

The thermal accommodation coefficient α_t is evaluated by using MD simulations in the following way. Equation (28) is rewritten as

$$\alpha_t = \frac{T_c - T_r}{T_c - T_\ell}, \tag{33}$$

where T_ℓ is prescribed (here at 85 K), T_c can be evaluated by Eq. (29) in the region $2 < z^* < 4$ (see Table I), and T_r is taken from Eq. (27) by rearrangement,

$$T_r = \frac{\alpha_e \rho_v}{(1-\alpha_c)\sigma_w}(T_t - T_\ell) + T_t. \tag{34}$$

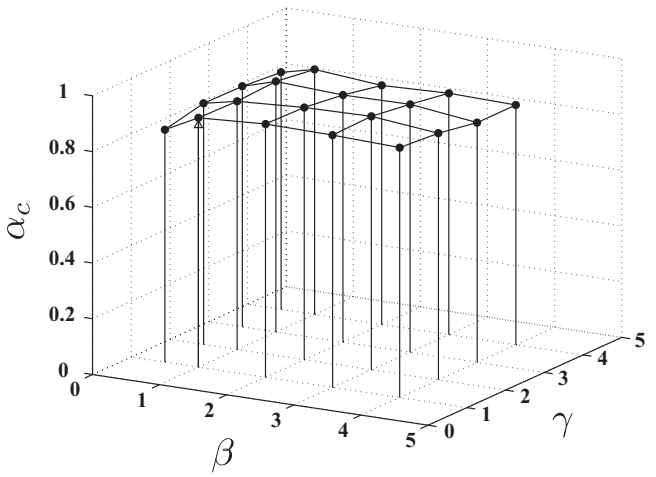

FIG. 5. The condensation coefficient α_c in nonequilibrium states at $T_\ell = 85$ K. The open triangle denotes the evaporation coefficient estimated in the previous study [37].

T_r is now known because all the quantities on the right-hand side of Eq. (34) are obtained by MD simulations including T_t. Thus α_t can be obtained via Eq. (33).

Figure 6(a) shows the thermal accommodation coefficient α_t calculated from the present MD simulations (the values of which are listed in Table I), where the values of α_t for $\gamma = 1.0$ are omitted because $T_c \sim T_\ell$ in the case of $\gamma = 1.0$, and the denominator of the right-hand side of Eq. (33) approaches zero, indicating that α_t is indefinite. One can see that α_t decreases with increasing β, whereas α_t is insensitive to changes of γ. This fact is clearly seen in the two-dimensional plot of Fig. 6(b), which is the projection of Fig. 6(a) onto the (β,α_t) plane. In the limit of $\beta \to 0$, α_t seems to approach unity; i.e., complete accommodation is obtained. This means that the KBC approaches the widely used isotropic form [12–14] in the limit of $\beta \to 0$:

$$f^{\rm out} = [\alpha_e \rho_v + (1-\alpha_c)\sigma_w]\hat{f}_x^*(T_\ell)\hat{f}_y^*(T_\ell)\hat{f}_z^*(T_\ell) \quad (\xi_z > 0). \tag{35}$$

Note that this form is also valid approximately near the equilibrium state since T_t approaches T_ℓ. When β increases, however, the interface tends to become unstable since most incident molecules condense onto the interface and some finite time may be required to accommodate the liquid temperature T_ℓ completely. Thus the energy relaxation is insufficient for larger β. We further discuss the energy relaxation and its anisotropic behavior in the following sections.

For the purpose of an actual application of the KBC, we provide a fitting function for α_t as a function of β as

$$\alpha_t = \exp(-k_t \beta), \tag{36}$$

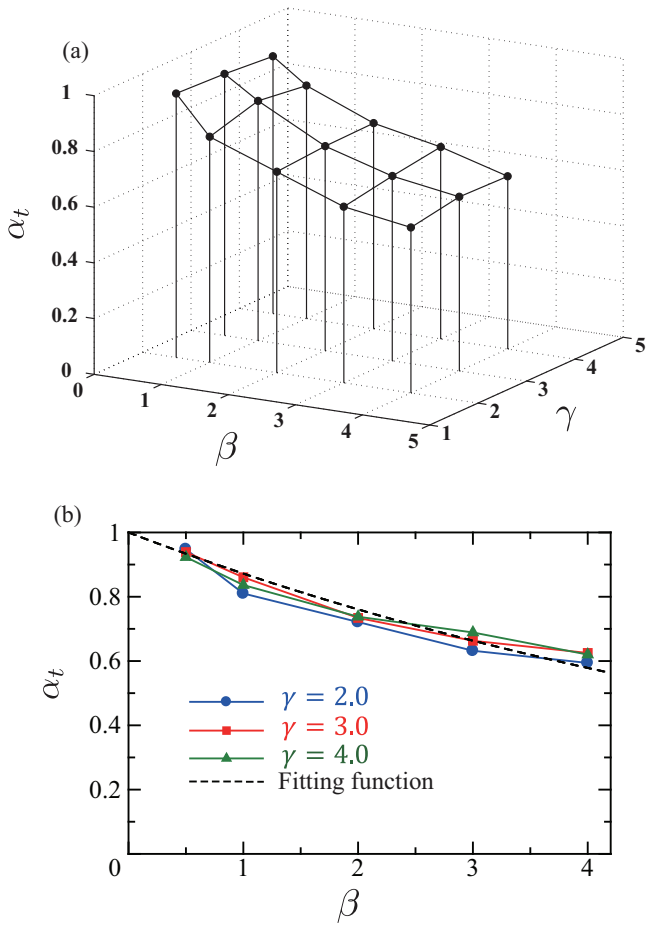

FIG. 6. (Color online) The thermal accommodation coefficient α_t in nonequilibrium states at $T_\ell = 85$ K. Note that data for $\gamma = 1.0$ are omitted since α_t is indefinite (see the text). (a) The three-dimensional plot for α_t as a function of (β,γ) sets, and (b) its projection onto the (β,α_t) plane. The dotted line in (b) is the fitting function Eq. (36).

where k_t is a parameter, and β is obtained from Eq. (31) to be

$$\beta = \frac{\int_{\xi_z<0} f^{\rm coll} d\boldsymbol{\xi}}{\int_{\xi_z<0} f^*(T_\ell) d\boldsymbol{\xi}} = \frac{\sigma^{\rm coll}}{\rho_v}. \tag{37}$$

In Eq. (37), $f^*(T_\ell)$ is the Maxwell VDF of saturated vapor at T_ℓ. The least-squares-fitted value of k_t is 0.137 for argon at 85 K. In Fig. 6(b), the fitting function Eq. (36) is plotted. The thermal accommodation coefficient α_t is now known, from which T_r and then T_t can be evaluated by Eqs. (28) and (27), with T_c being prescribed.

In Sec. IV G and the Appendix, the temperature dependence of k_t will be discussed.

E. Tangential component of the velocity distribution function

In Sec. IV B, we obtained the result that $f^{\rm out}$ can be expressed in the functional form of Eq. (10), i.e., as a product of the reduced VDFs at the tangential temperature T_t $(\neq T_\ell)$ and at the perpendicular temperature T_ℓ. This manifests that the molecular velocity component normal to the interface is completely accommodated, whereas the tangential velocity component is not. Here, we discuss the molecular mechanism of the inhomogeneity of the three-dimensional velocity distribution by further analyzing MD simulations.

First, we speculate that the relaxation times of the molecular velocities normal and tangential to the interface are different. That is, the normal velocity component ξ_z of molecules incident on the interface is rapidly relaxed, whereas their tangential velocity components ξ_x and ξ_y are slowly relaxed in the anisotropic environment of the transition region. Qualitatively, this picture may be valid because ξ_z of incident molecules must be reversed if the molecules are to be reemitted, i.e., strong interaction has to take place, whereas ξ_x and ξ_y do not have to be reversed. This indicates that ξ_z is easily relaxed at the liquid temperature T_ℓ, whereas the initial values of ξ_x and ξ_y can be retained to a certain extent. The following analysis actually supports this picture.

1. *Analysis of the time correlation function of molecular velocity*

Now we introduce the velocity autocorrelation function (VAF) of the molecular velocity $\boldsymbol{\xi}_i$ of the ith molecule as

$$C_{\xi\xi}(t) = \langle \boldsymbol{\xi}_i(0) \cdot \boldsymbol{\xi}_i(t) \rangle, \tag{38}$$

where $\boldsymbol{\xi}_i = (\xi_{x,i}, \xi_{y,i}, \xi_{z,i})$. From the Green-Kubo relation, we have the self-diffusion coefficient from $C_{\xi\xi}(t)$: $D_s = \int_0^\infty C_{\xi\xi}(t)\, dt$ [51]. From Eq. (38), we have the x and z components of $C_{\xi\xi}(t)$ as

$$C_{\xi\xi,x}(t) = \langle \xi_{x,i}(0) \xi_{x,i}(t) \rangle, \tag{39a}$$

$$C_{\xi\xi,z}(t) = \langle \xi_{z,i}(0) \xi_{z,i}(t) \rangle. \tag{39b}$$

We pay attention to these two components only, because $C_{\xi\xi,x}(t) = C_{\xi\xi,y}(t)$. The normalized VAF is defined as $\hat{C}_{\xi\xi}(t) = C_{\xi\xi}(t)/C_{\xi\xi}(0)$, where $\lim_{t\to 0} \hat{C}_{\xi\xi}(t) = 1$ and $\lim_{t\to\infty} \hat{C}_{\xi\xi}(t) = 0$. To estimate the relaxation time τ_ι of the molecular velocity components, $\hat{C}_{\xi\xi,\iota}(t)$ is fitted with the following function:

$$\hat{C}_{\xi\xi,\iota}(t) = \exp\left(-\frac{t}{\tau_\iota}\right) \quad (\iota = x \text{ or } y). \tag{40}$$

To analyze the relaxation time of the molecular velocity as a function of interfacial depth in the z direction, we introduce the following VAF:

$$C_{\xi\xi,\iota}(t,z) = \langle \xi_{\iota,i}(0) \xi_{\iota,i}(t) \delta(z - z_i(0)) \rangle \quad (\iota = x \text{ or } z), \tag{41}$$

where $z_i(t)$ is the z position of the ith molecule at time t. The time correlation functions were calculated according to the algorithm in Ref. [50].

Figure 7 shows the normalized VAF tangential (thick red lines) and normal (thin blue lines) to the interface, $\hat{C}_{\xi\xi,\iota}(t, z^* = -1.75)$ (liquid) and $\hat{C}_{\xi\xi,\iota}(t, z^* = 1.75)$ (interface), $\iota = x$ or z, defined in Eq. (41). Note that the initial molecular position z^* changes as time progresses due to molecular diffusion. Nevertheless, the qualitative behavior of the molecular velocity components in the liquid and in the interface (transition region) can be discriminated in Fig. 7. In the case of the interior of the liquid ($z^* = -1.75$), $\hat{C}_{\xi\xi,\iota}$ $(\iota = x \text{ or } z)$ rapidly decreases and converges to zero within $\sim$1 ps, whereas $\hat{C}_{\xi\xi,\iota}$ $(\iota = x \text{ or } z)$ slowly decreases in the transition region ($z^* = 1.75$). The rapid decrease in the liquid phase is due to the packing effect by surrounding molecules. The negative sign of $\hat{C}_{\xi\xi,\iota}$ $(\iota = x \text{ or } z)$ at about

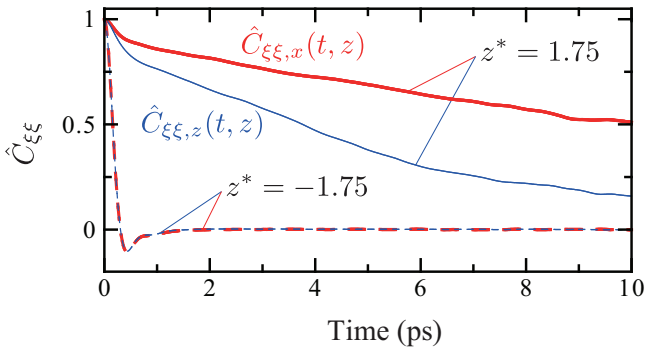

FIG. 7. (Color online) The time correlation function of molecular velocity tangential (thick red lines) and normal (thin blue lines) to the interface for the initial molecular positions $z^* = \pm 1.75$.

0.4 ps in the case of the interior of the liquid ($z^* = -1.75$) reveals the oscillating behavior of argon molecules in the liquid. The most important manifestation in Fig. 7 is that $\hat{C}_{\xi\xi,x}$ and $\hat{C}_{\xi\xi,z}$ are almost the same in the interior of the liquid ($z^* = -1.75$), while in the transition region ($z^* = 1.75$) the relaxation of $\hat{C}_{\xi\xi,z}$ is more rapid than that of $\hat{C}_{\xi\xi,x}$, clearly indicating the anisotropic relaxation of molecular velocity.

Shown in Fig. 8 are the relaxation times τ_x and τ_z of molecular velocity components [least-squares-fitted values of Eq. (40)] as a function of z^*. One can see that the relaxation time in the x direction, τ_x, deviates from that in the z direction, τ_z, in the transition region of $2 > z^* > 0$. In that region, τ_x is about three times larger than τ_z. These results are consistent with the molecular picture of an anisotropic relaxation stated at the beginning of this section.

2. *Analysis of the friction coefficient in Langevin dynamics*

Here we consider the anisotropic relaxation found in the preceding sections from another aspect, Langevin dynamics. Langevin dynamics enables us to trace a permeating molecule (a tagged molecule) among surrounding molecules as three-dimensional Brownian motion:

$$m\frac{d^2X(t)}{dt^2} = -\frac{\partial G(X,Y,Z)}{\partial x} - \gamma'_X(X,Y,Z)\frac{dX(t)}{dt} + R_X(X,Y,Z,t), \tag{42a}$$

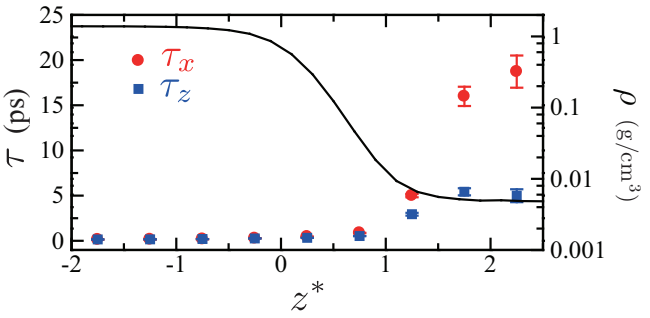

FIG. 8. (Color online) The relaxation time of molecular velocities tangential (red circles) and normal (blue squares) to the interface. The solid line indicates the density profile of the equilibrium state at 85 K.

$$m\frac{d^2Y(t)}{dt^2} = -\frac{\partial G(X,Y,Z)}{\partial y} - \gamma'_Y(X,Y,Z)\frac{dY(t)}{dt} + R_Y(X,Y,Z,t), \tag{42b}$$

$$m\frac{d^2Z(t)}{dt^2} = -\frac{\partial G(X,Y,Z)}{\partial z} - \gamma'_Z(X,Y,Z)\frac{dZ(t)}{dt} + R_Z(X,Y,Z,t), \tag{42c}$$

where X, Y, and Z are, respectively, the reaction coordinates in the x, y, and z directions for the tagged molecule, t is the time, m is the mass of the molecule, G is the potential of the mean force in the z direction, γ'_X, γ'_Y, and γ'_Z are, respectively, the space-dependent friction coefficients in the x, y, and z directions, and R_X, R_Y, and R_Z are random forces. We assume that molecular motions are homogeneous in the x and y directions; therefore Eqs. (42a) and (42b) are identical. The averaged potential of the mean force and the friction coefficients can be calculated by using MD simulations as functions of the coordinate Z. We will suppose that the Z coordinate of the tagged molecule is first fixed at a certain position of $Z = Z_0$ for Eqs. (42a) and (42c), and for Eq. (42a) the X coordinate is fixed during the MD simulations; the X and Y coordinates in Eq. (42c) and the Y coordinate in Eq. (42a) are allowed to move during the MD simulations. Then, by using the fluctuation-dissipation theorem [52,53], the following relations hold (see the Supplemental Materials [54]):

$$\gamma_z(Z_0,t) = \frac{1}{k_BT}[\langle F_z(Z_0,0)F_z(Z_0,t)\rangle - \langle F_z(Z_0)\rangle^2], \tag{43a}$$

$$\gamma_x(X_0,Z_0,t) = \frac{1}{k_BT}[\langle F_x(X_0,Z_0,0)F_x(X_0,Z_0,t)\rangle] \tag{43b}$$

and

$$\gamma'_z(Z_0) = \int_0^\infty \gamma_z(Z_0,t)\,dt, \tag{44a}$$

$$\gamma'_x(X_0,Z_0) = \int_0^\infty \gamma_x(X_0,Z_0,t)\,dt, \tag{44b}$$

where T is the system temperature (=85 K), $F_z(Z_0,t)$ is a force in the z direction at time t exerted on the tagged molecule at the fixed position $z = Z_0$, and $F_x(X_0,Z_0,t)$ is a force in the x direction at time t exerted on the tagged molecule at the fixed positions $x = X_0$ and $z = Z_0$. The symbol $\langle\ \rangle$ denotes the ensemble average. The dynamics of the tagged molecule in the liquid and in the vapor is well described by Eqs. (42a) and (42c), and here we calculate the friction coefficients near the interface in the x and z directions, γ'_x and γ'_z, respectively, in MD simulations by Eqs. (44a) and (44b).

Figure 9 shows the MD simulation result of the friction coefficients, where the dotted line denotes the friction coefficient of bulk liquid from the experimentally reported diffusion coefficient [55] ($D = 1.53 \times 10^{-9}$ m^2/s) and the Einstein relation $D = k_BT/\gamma'$. One can clearly see the existence of anisotropic friction near the interface. The friction coefficients monotonically increase from vapor to liquid. On the vapor side of the transition region ($-0.5 < z^*$), $\gamma'_z > \gamma'_x$, indicating that the friction normal to the interface is larger than the tangential component. This corresponds to a picture in which the molecular velocity normal to the interface is quickly

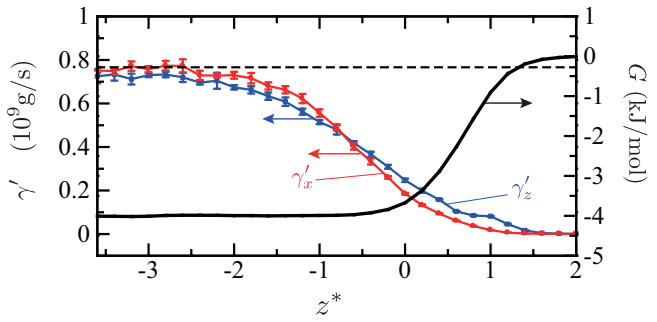

FIG. 9. (Color online) The space-dependent friction coefficient of argon near the vapor-liquid interface in the equilibrium state at 85 K. Red and blue lines denote γ'_x and γ'_z defined in Eqs. (43), respectively. The dashed line is the friction coefficient of bulk liquid estimated from the experimental diffusion coefficient and the Einstein relation (see text). The thick black line is the potential of the mean force G calculated from the thermodynamic integration method [50,51] (see also the Supplemental Materials [54]): $G(z) = -\int_{z_{\rm liq}}^{z_{\rm vap}} \langle F_z(z)\rangle_z dz$.

relaxed compared to the tangential velocity, which is consistent with the result of the multicomponent VDF for $f^{\rm out}$. On the liquid side of the interface ($z^* < -0.5$), the relation is reversed: $\gamma'_x > \gamma'_z$. This can be explained by the surface tension of the liquid, which is defined as the difference between normal pressure and tangential pressure [56]. In the liquid, the virial pressure always shows a minus sign due to the attractive interaction, and hence the positive surface tension of the liquid means that the tangential pressure is greater than the normal pressure in absolute value. This may lead to the fact that $\gamma'_x > \gamma'_z$.

Additionally, in Fig. 9, the calculated potential of the mean force G is plotted as a function of the interfacial depth z^*. One can see that G monotonically decreases from vapor to liquid and that the change of G occurs on the vapor side of the interface ($0 < z^* < 1$) rather than in the middle of the transition layer ($z^* \sim 0$). G has a constant value on the liquid side ($z^* < 0$), while the friction coefficients still change in the range of $-2 < z^* < 0$. This indicates that a molecule experiences diffusional processes different from those in the bulk region near the interface. The calculated ΔG value between vapor and liquid is -4.01 kJ/mol, a value consistent with those of other reports of the free energy for argon (e.g., see Ref. [57]).

Here we also notice that the calculated G has no potential barrier on the vapor side of the interface, which is consistent with the recent report on water evaporation by Varilly and Chandler [58]. This would indicate that the evaporation coefficient α_e (the condensation coefficient in the equilibrium state) should be unity [58]. However, in Sec. IV C, α_e in the present simulations exhibits a value of 0.868 (slightly smaller than unity). In the Appendix, we provide a fitting function for α_e as a decreasing function of T_ℓ. This discrepancy can be explained as follows: With increasing T_ℓ, the mass flux of the outgoing molecules tends to correlate with that of the incident molecules by phenomena such as "molecular exchange" [25]. In our definition of $f^{\rm out}$ given in Eq. (5), the part of the outgoing molecules influenced by incident molecules is classified as the component of reflection. This is the reason why our simulations indicate that α_e has a value smaller than unity even though the potential of the mean force has no distinct barrier.

F. Mechanism of the behavior of α_t

In the preceding sections, we have seen the multicomponent VDF for $f^{\rm out}$ with the tangential directions being characterized by the tangential temperature T_t, and we have discussed its

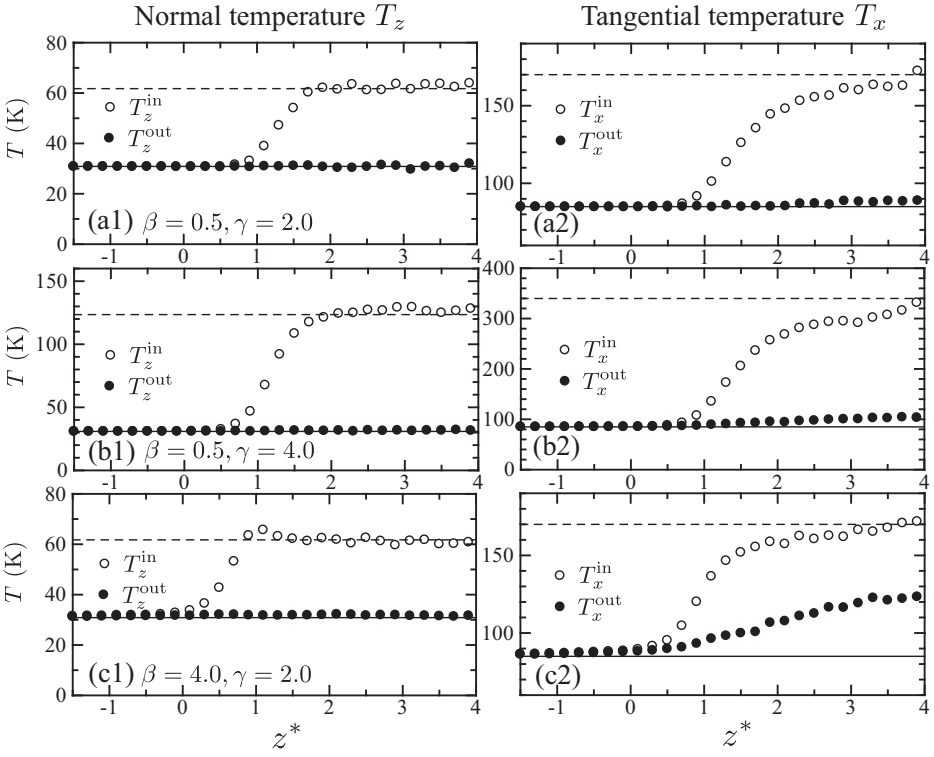

FIG. 10. Temperature profile of molecules incident onto and outgoing from the interface. The upper, middle, and lower graphs show the results of simulations for ($\beta = 0.5, \gamma = 2.0$), ($\beta = 0.5, \gamma = 4.0$), and ($\beta = 4.0, \gamma = 2.0$), respectively. The left and the right panels are the normal and the tangential components, respectively. The open (filled) circles are the temperatures of molecules incident onto (outgoing from) the interface $T_\iota^{\rm in}$ ($T_\iota^{\rm out}$), calculated from $\int_{\xi_z<(>)0} \xi_\iota^2 f d\boldsymbol{\xi}/(\rho R)$ ($\iota = x$ or z). The dashed lines indicate the temperatures estimated from $f^{\rm coll}(\beta,\gamma)$ [Eq. (31)], which become γT_ℓ for $\iota = x$ and $\gamma(1-2/\pi)T_\ell$ for $\iota = z$, respectively. The solid lines indicate the temperatures estimated from the reduced Maxwell velocity distribution at T_ℓ, which become T_ℓ for $\iota = x$ and $(1-2/\pi)T_\ell$ for $\iota = z$, respectively (see the text for details).

mechanism. The tangential temperature T_t is formulated by the thermal accommodation coefficient α_t in Sec. II, and the present MD simulations show that α_t is a decreasing function of the parameter β specifying the density of the incident molecules, whereas it is only slightly dependent on γ specifying the temperature of the incident molecules. This indicates that a reflected molecule is less accommodated thermally to the liquid temperature if the nonequilibrium vapor has a higher density compared to the saturated vapor density. In this section, we discuss a molecular mechanism for this β dependency of α_t.

To observe the behavior of the tangential and the normal temperatures for $f^{\rm out}$ influenced by $f^{\rm coll}$ in detail, the temperature profiles of molecules incident onto and outgoing from the interfaces are shown in Fig. 10. The results of three nonequilibrium simulations are compared in the figure: the upper graphs show the normal temperature T_z [Fig. 10(a1)] and the tangential temperature T_x [Fig. 10(a2)] in the simulation of $f^{\rm coll}(\beta=0.5,\gamma=2.0)$, the middle ones [Figs. 10(b1 and 10(b2)] show those in the simulation of $f^{\rm coll}(\beta=0.5,\gamma=4.0)$ to see the γ dependence of the results, and the lower ones [Figs. 10(c1) and 10(c2)] show those in the simulation of $f^{\rm coll}(\beta=4.0,\gamma=2.0)$ to see the β dependence of the results. The open (filled) circles are the temperatures of molecules incident onto (outgoing from) the interface $T_\iota^{\rm in}$ ($T_\iota^{\rm out}$), calculated by [see Eq. (18)] $\int_{\xi_z<(>)0}(\xi_\iota - v_\iota)^2 f d\boldsymbol{\xi}/(\rho R)$ for $\iota = x$ or z. The dotted lines indicate the temperatures estimated from $f^{\rm coll}(\beta,\gamma)$ [see Eq. (31)]: $\int_{\xi_z<0}\xi_\iota^2 f^{\rm coll} d\boldsymbol{\xi}/(\sigma^{\rm coll} R)$ for $\iota = x$ or z, which become γT_ℓ for $\iota = x$ and $\gamma(1-2/\pi)T_\ell$ for $\iota = z$. The solid lines indicate the temperatures estimated from the reduced Maxwell VDF at T_ℓ, $f^*(T_\ell)$: $\int_{\xi_z>0}(\xi_\iota - v_\iota)^2 f^* d\boldsymbol{\xi}/(R)$ for $\iota = x$ or z, which become T_ℓ for $\iota = x$ and $(1-2/\pi)T_\ell$ for $\iota = z$.

First, we focus on Figs. 10(a1), 10(b1), and 10(c1). $T_z^{\rm in}$ (open circles) in the vapor region $z^* > 2.0$ well corresponds to the dotted lines, and the profiles gradually decrease to the values characterized by the liquid temperature when going from vapor to liquid in the transition region, and finally the temperatures become homogeneous in the liquid. $T_z^{\rm out}$ (filled circles), on the other hand, is homogeneous in all regions. These results indicate that $f^{\rm out}$ is hardly influenced by $f^{\rm coll}$, and the marginal distribution $\hat{f}_z$ becomes the reduced Maxwell VDF at T_ℓ, $\hat{f}^*(T_\ell)$, resulting in complete thermal accommodation $\alpha_t = 1$. Next, we focus on Figs. 10(a2), 10(b2), and 10(c2). In the case of $f^{\rm coll}(\beta=0.5,\gamma=2.0)$ [Fig. 10(a2)], $T_x^{\rm out}$ (filled circles) is hardly influenced by the incident temperature $T_x^{\rm in}$, similarly to the case of the normal (perpendicular) temperature. In the case of $f^{\rm coll}(\beta=0.5,\gamma=4.0)$ [Fig. 10(b2)], the qualitative behavior is the same as in the case of $f^{\rm coll}(\beta=0.5,\gamma=2.0)$, even though $T_x^{\rm in}$ in Fig. 10(b2) is twice as large as that in Fig. 10(a2). In the case of $f^{\rm coll}(\beta=4.0,\gamma=2.0)$ [Fig. 10(c2)], however, $T_x^{\rm out}$ is strongly shifted by the influence of $T_x^{\rm in}$, and a temperature gradient can be seen in the region near the interface. This temperature gradient in the transition region for $T_x^{\rm out}$ leads to the decrease of α_t. Now we have a physical picture for the molecular interaction in the transition layer being strongly anisotropic.

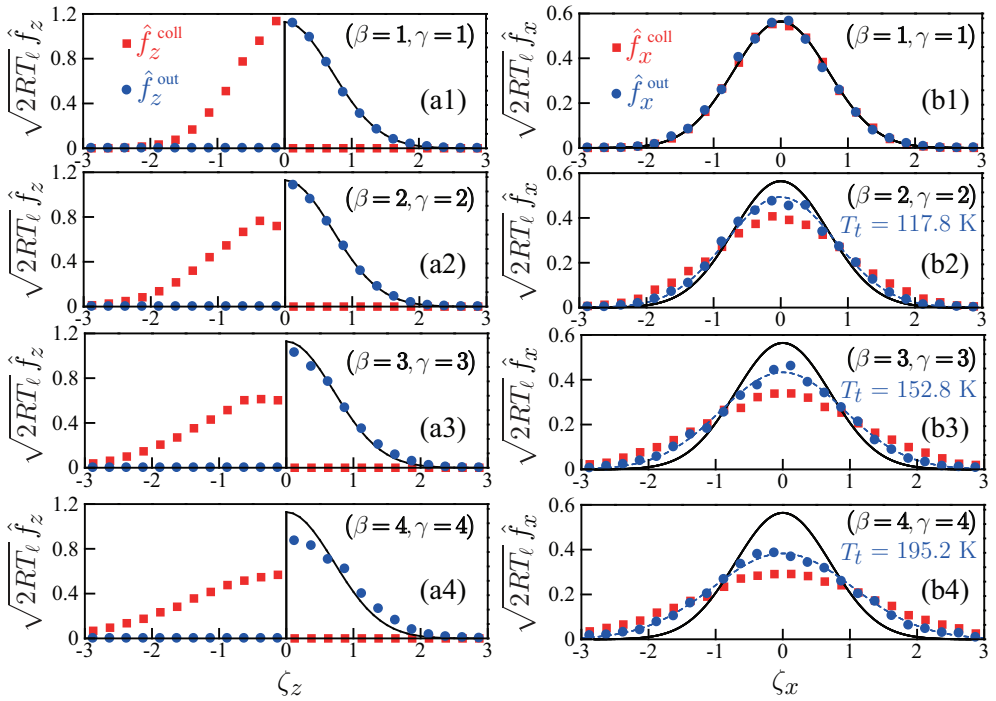

FIG. 11. (Color online) Normalized velocity distribution function of molecules incident onto the interface, $\hat{f}^{\rm coll}$ (red squares), and outgoing from the interface, $\hat{f}^{\rm out}$ (blue circles), calculated in MD simulations at $T_\ell = 90$ K, where $\zeta_\iota = \xi_\iota/\sqrt{2RT_\ell}$ ($\iota = x,z$). The solid curves in the left panels denote one-dimensional, normalized reduced half-Maxwell velocity distributions with T_ℓ (=90 K): $(2/\sqrt{\pi})\exp(-\zeta_z^2)$ $(\zeta_z > 0)$; those in the right panels denote one-dimensional, normalized reduced Maxwell velocity distributions with T_ℓ: $(1/\sqrt{\pi})\exp(-\zeta_x^2)$. The dotted curves in the right panels are one-dimensional, normalized reduced Maxwell velocity distributions with different temperatures T_t: $\sqrt{T_\ell/(T_t\pi)}\exp(-\zeta_x^2 T_\ell/T_t)$.

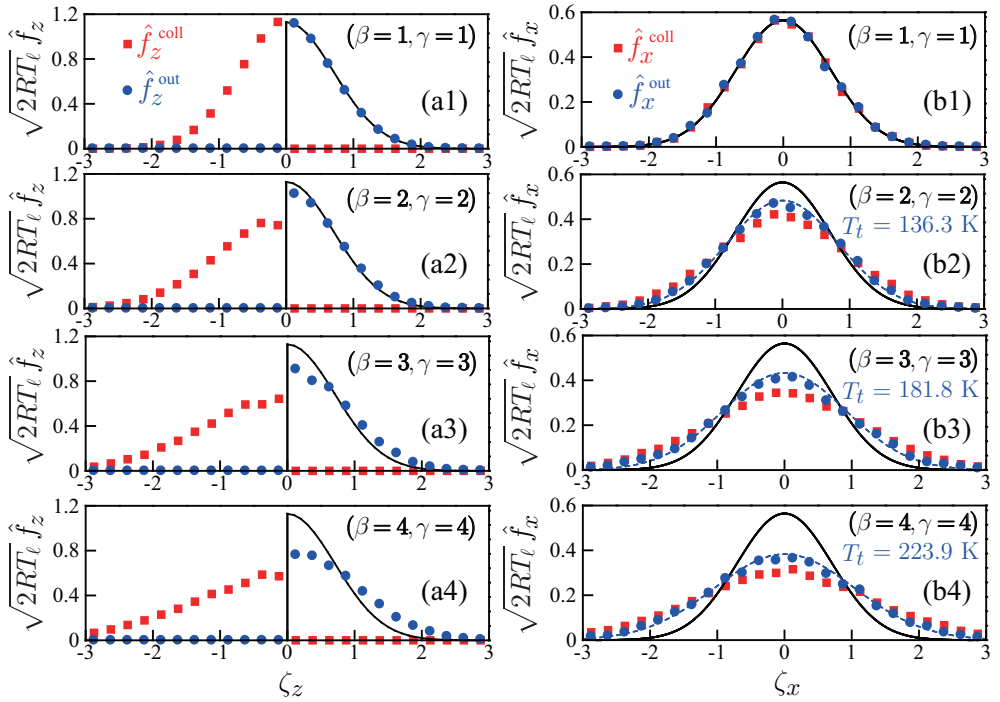

FIG. 12. (Color online) Normalized velocity distribution function of molecules incident onto the interface, $\hat{f}^{\rm coll}$ (red squares), and outgoing from the interface, $\hat{f}^{\rm out}$ (blue circles), calculated in MD simulations at $T_\ell = 100$ K, where $\zeta_\iota = \xi_\iota/\sqrt{2RT_\ell}$ ($\iota = x,z$). The solid curves in the left panels denote one-dimensional, normalized reduced half-Maxwell velocity distributions with T_ℓ (=100 K): $(2/\sqrt{\pi})\exp(-\zeta_z^2)$ ($\zeta_z > 0$); those in the right panels denote one-dimensional, normalized reduced Maxwell velocity distributions with T_ℓ: $(1/\sqrt{\pi})\exp(-\zeta_x^2)$. The dotted curves in the right panels are one-dimensional, normalized reduced Maxwell velocity distributions with different temperatures T_t: $\sqrt{T_\ell/(T_t\pi)}\exp(-\zeta_x^2 T_\ell/T_t)$.

Here we consider the reason why α_t is affected by the vapor state (especially β). In Sec. IV E2, we discussed the reason why α_e and α_c are smaller than unity in spite of the barrierless process: an incident molecule tends to stick to the interface without reflection, and alternatively other molecules staying near the interface are influenced by an incident molecule, effectively increasing the mass flux of reflection. This kind of correlation effect can also explain the behavior of α_t. If ξ_z of an incident molecule is rapidly relaxed at T_ℓ as demonstrated in the previous section, there may be no correlation between ξ_z of an incident molecule and ξ_z of a reflected molecule. In the case of molecular velocity tangential to the interface, our analysis showed a slow relaxation to T_ℓ, indicating that ξ_x (or ξ_y) of the reflected component tends to be affected by the incident molecules. This produces a non-negligible gradient for $T_x^{\rm out}$ in the interfacial region discussed above, which accounts for

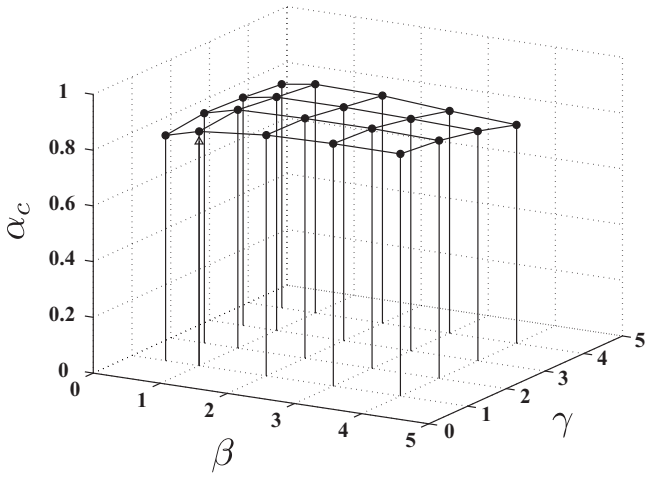

FIG. 13. The condensation coefficient α_c in nonequilibrium states at $T_\ell = 90$ K. The open triangle denotes the evaporation coefficient estimated in the previous study [37].

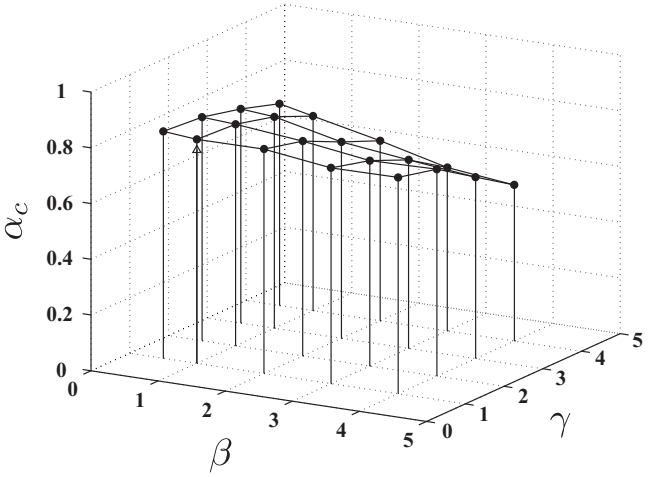

FIG. 14. The condensation coefficient α_c in nonequilibrium states at $T_\ell = 100$ K. The open triangle denotes the evaporation coefficient estimated in the previous study [37].

the reason why α_t shows a β dependence in the present MD simulation.

G. T_ℓ dependence of the KBC

In an application of the present KBC to actual heat and mass transfer problems, one often needs to treat unsteady states, in which the temperature changes in time. Thus, in this section, we examine the dependence of the KBC on the temperature of the condensed phase, T_ℓ. The methodology of MD simulation and the analysis are essentially the same as in the previous sections, and some remarks on the MD procedures and the numerical values of the simulation data are described in the Supplemental Materials [54].

The normalized VDFs of outgoing molecules, $\hat{f}^{\rm out}$, at $T_\ell = 90$ K as a function of β and γ are shown in Fig. 11. In comparison with the case of $T_\ell = 85$ K in Fig. 4, the qualitative features are the same in the case of $\beta = \gamma = 1,2,3$; that is, the normal VDFs (blue circles) are well fitted with the (half) Gaussian distribution at T_ℓ, while the tangential VDFs deviate from the Gaussian distribution at T_ℓ, though the degree of the deviation may be different for $T_\ell = 85$ K and $T_\ell = 90$ K. We will return to the temperature dependence of the thermal accommodation coefficient in a later discussion. A noticeable feature can be seen in Fig. 11(a4); $\hat{f}_z^{\rm out}$ in the case of $\beta = \gamma = 4$ deviates from the (half) Gaussian distribution and shifts to a Gaussian at a higher temperature than T_ℓ. This feature can be more clearly seen in the case of $T_\ell = 100$ K shown in Fig. 12. In the case of $\beta = \gamma = 3$ at $T_\ell = 100$ K [Fig. 12(a3)], $\hat{f}_z^{\rm out}$ has already deviated from the Gaussian at T_ℓ. This deviation indicates that not only does the thermal accommodation coefficient (α_t) tangential to the interface become less than unity but so does that normal to it. This may not be a surprising result because $\hat{f}_z^{\rm out}$ can be affected by the vapor in a strong nonequilibrium state. If $\hat{f}_z^{\rm out}$ deviates from the Gaussian at T_ℓ, Eq. (13) derived from the mass flux relationships fails to hold, and hence the deviation from T_ℓ (i.e., the deviation of the thermal accommodation coefficient for the normal velocity component from unity) can be regarded as an indication of the range of applicability of the present KBC, which is further discussed below. Nevertheless, even in the high-temperature cases, the present KBC still holds unless the vapor condition is very far from equilibrium.

Next, we focus on the condensation coefficient α_c in nonequilibrium states at two temperatures different from $T_\ell = 85$ K. Figures 13 and 14 show, respectively, α_c at $T_\ell = 90$ K and $T_\ell = 100$ K. In the case of $T_\ell = 90$ K, α_c has an almost constant value, being similar to the case of $T_\ell = 85$ K. In the case of $T_\ell = 100$ K, on the other hand, α_c decreases, especially in the high-γ and in the high-β cases. Fortunately, however, the treatment of constant α_c (i.e., $\alpha_c = \alpha_e$) in nonequilibrium states may still hold near equilibrium even in the high-temperature cases. In an actual application of the present KBC, one should bear in mind that such a treatment may fail in a strong nonequilibrium state. In the Appendix, we provide a fitting function for α_e as a function of T_ℓ for an actual application, which is derived from previous MD simulation results [37,43].

Lastly, we shall discuss the temperature dependence of the thermal accommodation coefficient α_t for the tangential velocity component. In Figs. 15 and 16, α_t values in the nonequilibrium states at $T_\ell = 90$ K and $T_\ell = 100$ K are shown, respectively. The qualitative features are the same as in the case of $T_\ell = 85$ K shown in Fig. 6; α_t is a decreasing function of β, while it is less affected by γ. The least-squares fitting of the data to the function of Eq. (36) [Figs. 15(b) and 16(b)] leads to $k_t = 0.183$ at $T_\ell = 90$ K and $k_t = 0.269$ at $T_\ell = 100$ K. Figure 17 shows k_t as a function of T_ℓ, indicating that the present data are well fitted with a linear function of T_ℓ. In the Appendix, we also provide the least-squares-fitted function for an actual application.

Shown in Fig. 18 is the thermal accommodation coefficient for the normal velocity component at $T_\ell = 85$, 90, and 100 K, where the data were evaluated based on Eq. (33) for the normal temperatures given by Eqs. (18) and (23) (with numerical values of the data being tabulated in the Supplemental Materials [54]). One can clearly recognize that $\alpha_t \approx 1$ holds at $T_\ell = 85$ K, and also at $T_\ell = 90$ K, whereas it decreases with increasing β at $T_\ell = 100$ K, which is qualitatively the same as the case of the tangential velocity component discussed above. We again notice that the deviation of the value from unity is an indication of the range of applicability of the present KBC. Fortunately, the deviation may not be serious compared to the

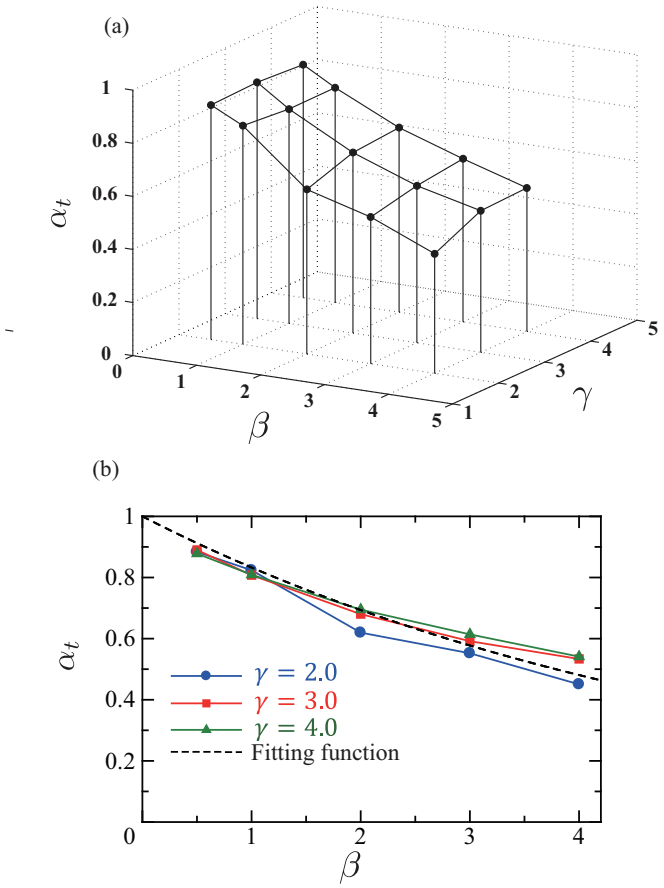

FIG. 15. (Color online) The thermal accommodation coefficient α_t in nonequilibrium states at $T_\ell = 90$ K. Note that data for $\gamma = 1.0$ are omitted since α_t is indefinite (see the text). (a) The three-dimensional plot for α_t as a function of (β,γ) sets, and (b) its projection onto the (β,α_t) plane. The dotted line in (b) is the fitting function Eq. (36).

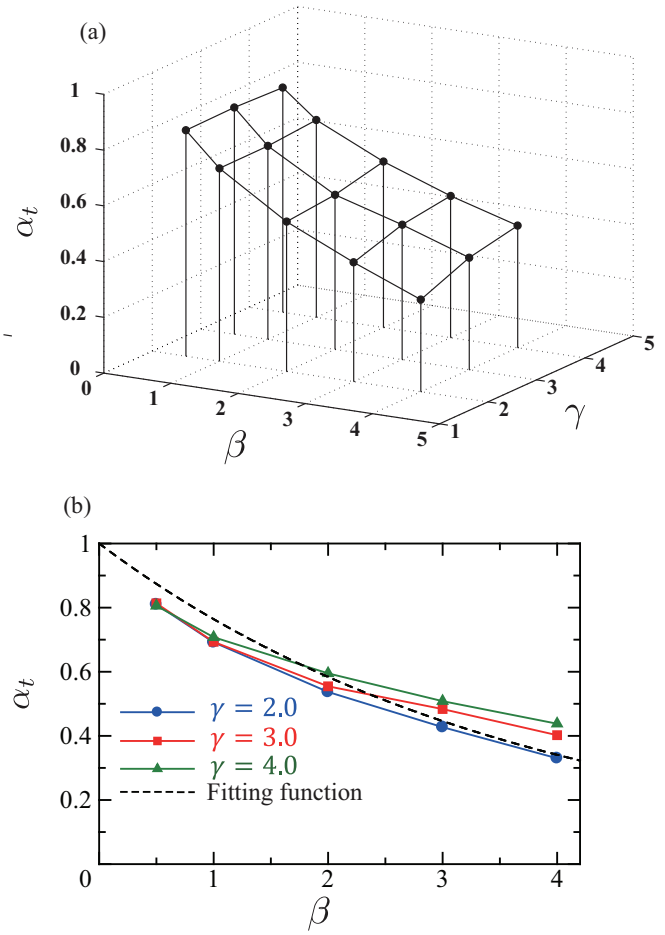

FIG. 16. (Color online) The thermal accommodation coefficient α_t in nonequilibrium states at $T_\ell = 100$ K. Note that data for $\gamma = 1.0$ are omitted since α_t is indefinite (see the text). (a) The three-dimensional plot for α_t as a function of (β,γ) sets, and (b) its projection onto the (β,α_t) plane. The dotted line in (b) is the fitting function Eq. (36).

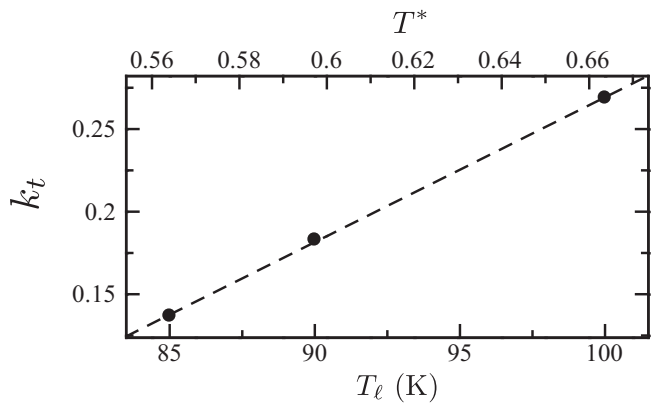

FIG. 17. The fitting parameter k_t in Eq. (36) for the thermal accommodation coefficient α_t as a function of the temperature T_ℓ. T^* is the reduced temperature defined by Eq. (A1), and the dotted line is the fitting function Eq. (A3).

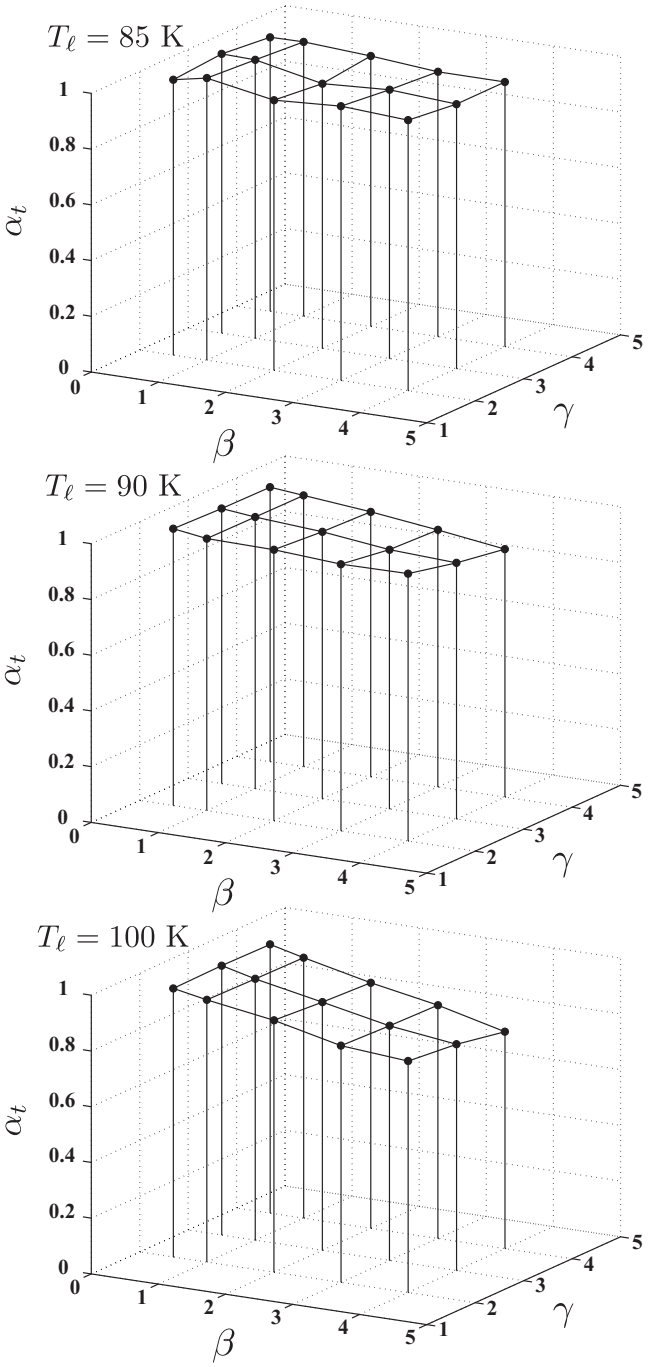

FIG. 18. The thermal accommodation coefficient for the normal velocity component at $T_\ell = 85$, 90, and 100 K.

case of α_t for the tangential velocity component. Surely, the difference in the thermal accommodation coefficient between tangential versus normal velocity components stems from the anisotropic relaxation of molecular velocities discussed in Sec. IV E.

V. CONCLUSIONS

In this study, a modeling procedure for a KBC at a vapor-liquid interface has been demonstrated, and a physically correct form of the KBC at the vapor-liquid interface of argon

near its triple point temperature, which covers a wide range of nonequilibrium vapor states, has been derived. The present KBC includes evaporation and condensation coefficients that specify the mass transfer and the thermal accommodation coefficient that specifies the energy transfer at an interface. When the VDF of molecules incident on an interface, $f^{\rm coll}$, is given, the VDF of molecules outgoing from the interface, $f^{\rm out}$, is uniquely determined. The MD simulations show that $f^{\rm out}$ has the functional form of the multicomponent VDF as given by Eq. (10) and that it approaches the Maxwell VDF at the liquid temperature, Eq. (35), as the number of incident molecules decreases. It was also found that the evaporation and the condensation coefficients are almost constant in a wide range of nonequilibrium states, while the thermal accommodation coefficient is a decreasing function of the density of incident molecules. The molecular mechanism of why the tangential temperature of $f^{\rm out}$ deviates from the liquid temperature was discussed. The analysis of velocity autocorrelation functions and friction coefficients clearly showed the anisotropic relaxation of incident molecules at the interface and that the tangential relaxation is slow while the normal one is rapid.

KBC studies for other substances [59–61] such as water [43] and mixtures [62] (for instance, of water and argon) will be required to apply the KBC to actual problems (e.g., the hybrid Rayleigh-Plesset molecular dynamics model [63] for bubble dynamics). These studies are now in progress.

ACKNOWLEDGMENTS

We are grateful to Professor Takeru Yano at Osaka University, Japan, for helpful discussions. This work was supported by Grants-in-Aid by the Ministry of Education, Culture, Sports, Science, and Technology (MEXT), Japan. A part of this work was performed at the Third Physical Institute, University of Göttingen, while the second author (S.F.) received support as a senior research fellow of the Alexander von Humboldt (AvH) Foundation, Federal Republic of Germany.

APPENDIX: FITTING FUNCTIONS OF α_e (α_c IN THE EQUILIBRIUM STATE) AND α_t AS A FUNCTION OF T_ℓ

In this Appendix, we shall provide a fitting function for the evaporation coefficient α_e, which is equal to the condensation coefficient in the equilibrium states by the definition of Eqs. (8), to apply the present KBC to an actual problems. In Ref. [64], α_e values of argon [37], water [43], and methanol [43] calculated in MD simulations were found to agree well with each other at the reduced temperature T^* defined as

$$T^* = \frac{T_\ell}{T_{\rm critical}}, \tag{A1}$$

where $T_{\rm critical}$ is the critical temperature (which, in the case of argon, is 150.7 K). As shown in Fig. 19, the data are well fitted with the following function:

$$\alpha_e = \log_{10}(B_1 - B_2(T^* - B_3)) + B_4. \tag{A2}$$

The least-squares fit [65] leads to the following values of B: $B_1 = 0.6795$, $B_2 = 1.9757$, $B_3 = 0.6608$, and $B_4 = 0.9403$ for $T^* > 0.424$.

In the case of α_t, the fitting function of Eq. (36) was found by introducing the parameter k_t, and in Fig. 17, k_t was found to be well fitted with a linear function of T^* as

$$k_t = B_5 T^* - B_6, \tag{A3}$$

where $B_5 = 1.322$ and $B_6 = 0.6077$ are derived by a least-squares fit for argon.

Note that the values of B may depend on the substances employed.

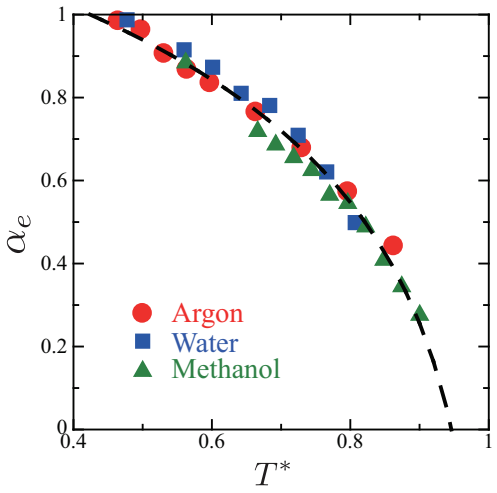

FIG. 19. (Color online) The evaporation coefficient α_e, which equals the condensation coefficient in the equilibrium state, for argon [37], water [43], and methanol [43], as a function of the reduced temperature T^*. The dotted line is the fitting function Eq. (A2).

[1] P. A. Thompson and S. M. Troian, Nature (London) **389**, 360 (1997).
[2] M. Cieplak, J. Koplik, and J. R. Banavar, Phys. Rev. Lett. **86**, 803 (2001).
[3] C. Denniston and M. O. Robbins, Phys. Rev. Lett. **87**, 178302 (2001).
[4] T. Qian, X. P. Wang, and P. Sheng, Phys. Rev. Lett. **93**, 094501 (2004).
[5] S. Kjelstrup and D. Bedeaux, *Non-equilibrium Thermodynamics of Heterogeneous Systems* (World Scientific, London, 2008).
[6] B. C. Garrett, G. K. Schenter, and A. Morita, Chem. Rev. **106**, 1355 (2006).
[7] S. Fujikawa, T. Yano, and M. Watanabe, *Vapor-Liquid Interfaces, Bubbles and Droplets* (Springer-Verlag, Heidelberg, 2011).
[8] W. Lauterborn and T. Kurz, Rep. Prog. Phys. **73**, 106501 (2010).
[9] S. Fujikawa and T. Akamatsu, J. Fluid Mech. **97**, 481 (1980).
[10] I. Akhatov, O. Lindau, A. Topolnikov, R. Mettin, N. Vakhitova, and W. Lauterborn, Phys. Fluids **13**, 2805 (2001).

[11] D. Fuster, G. Hauke, and C. Dopazo, J. Acoust. Soc. Am. **128**, 5 (2010).
[12] C. Cercignani, *Rarefied Gas Dynamics* (Cambridge University Press, New York, 2000).
[13] Y. Sone, *Kinetic Theory and Fluid Dynamics* (Birkhäuser, Boston, 2002).
[14] Y. Sone, *Molecular Gas Dynamics* (Birkhäuser, Boston, 2007).
[15] T. Yano, Fluid Dyn. Res. **40**, 474 (2008).
[16] S. Kosuge and Y. Okumura, AIP Conf. Proc. **1084**, 641 (2008).
[17] H. Hertz, Ann. Phys. Chem. **17**, 177 (1882).
[18] M. Knudsen, Ann. Phys. Chem. **47**, 697 (1915).
[19] A. Frezzotti, Phys. Fluids **23**, 030609 (2011).
[20] P. Davidovits, C. E. Kolb, L. R. Williams, J. T. Jayne, and D. R. Worsnop, Chem. Rev. **106**, 1323 (2006).
[21] S. Fujikawa, T. Yano, K. Kobayashi, K. Iwanami, and M. Ichijo, Exp. Fluids **37**, 80 (2004).
[22] K. Kobayashi, S. Watanabe, D. Yamano, T. Yano, and S. Fujikawa, Fluid Dyn. Res. **40**, 585 (2008).
[23] E. Mortensen and H. Eyring, J. Phys. Chem. **64**, 846 (1960).
[24] M. Matsumoto, Fluid Phase Equilib. **114**, 307 (1998).
[25] M. Matsumoto, K. Yasuoka, and Y. Kataoka, J. Chem. Phys. **101**, 7912 (1994).
[26] R. Meland, J. Chem. Phys. **117**, 7254 (2002).
[27] T. Tsuruta and G. Nagayama, J. Phys. Chem. B **108**, 1736 (2004).
[28] A. Frezzotti and T. Ytrehus, Phys. Fluids **18**, 027101 (2006).
[29] R. Holyst and M. Litniewski, Phys. Rev. Lett. **100**, 055701 (2008).
[30] A. Morita and B. C. Garrett, Fluid Dyn. Res. **40**, 459 (2008).
[31] K. Gu, C. B. Watkins, and J. Koplik, Phys. Fluids **22**, 112002 (2010).
[32] S. Takahama and L. M. Russell, J. Geophys. Res. **116**, D02203 (2011).
[33] S. Cheng, J. B. Lechman, S. J. Plimpton, and G. S. Grest, J. Chem. Phys. **134**, 224704 (2011).
[34] J. Julin, M. Shiraiwa, R. E. H. Miles, J. P. Reid, U. Pöschl, and I. Riipinen, J. Phys. Chem. A **117**, 410 (2012).
[35] S. I. Anisimov, D. O. Dunikov, S. P. Malyshenko, and V. V. Zhakhovskii, J. Chem. Phys. **110**, 8722 (1999).
[36] A. Frezzotti, L. Gibelli, and S. Lorenzani, Phys. Fluids **17**, 012102 (2005).
[37] T. Ishiyama, T. Yano, and S. Fujikawa, Phys. Fluids **16**, 2899 (2004).
[38] C. D. Cappa, W. S. Drisdell, J. D. Smith, R. J. Saykally, and R. C. Cohen, J. Phys. Chem. B **109**, 24391 (2005).
[39] J. D. Smith, C. D. Cappa, W. S. Drisdell, R. C. Cohen, and R. J. Saykally, J. Am. Chem. Soc. **128**, 12892 (2006).
[40] N. Musolino and B. L. Trout, J. Chem. Phys. **138**, 134707 (2013).
[41] M. Zientara, D. Jakubczyk, M. Litniewski, and R. Holyst, J. Phys. Chem. C **117**, 1146 (2013).
[42] R. Holyst, M. Litniewski, D. Jakubczyk, K. Kolwas, M. Kolwas, K. Kowalski, S. Migacz, S. Palesa, and M. Zientara, Rep. Prog. Phys. **76**, 034601 (2013).
[43] T. Ishiyama, T. Yano, and S. Fujikawa, Phys. Fluids **16**, 4713 (2004).
[44] T. Ishiyama, T. Yano, and S. Fujikawa, Phys. Rev. Lett. **95**, 084504 (2005).
[45] G. Nagayama and T. Tsuruta, J. Chem. Phys. **118**, 1392 (2003).
[46] M. Zientara, D. Jakubczyk, K. Kolwas, and M. Kolwas, J. Phys. Chem. A **112**, 5152 (2008).
[47] R. Holyst, M. Litniewski, D. Jakubczyk, M. Zientara, and M. Wozniak, Soft Matter **9**, 7766 (2013).
[48] G. A. Bird, *Molecular Gas Dynamics and the Direct Simulation of Gas Flows* (Oxford University Press, Oxford, 1994).
[49] A. W. Adamson and A. P. Gast, *Physical Chemistry of Surfaces*, 6th ed. (Wiley, New York, 1997).
[50] M. P. Allen and D. J. Tildesley, *Computer Simulation of Liquids* (Clarendon, Oxford, 1987).
[51] D. Frenkel and B. Smit, *Understanding Molecular Simulation* (Academic, New York, 1996).
[52] M. Toda, M. Saito, R. Kubo, and N. Hashitsume, *Statistical Physics II: Nonequilibrium Statistical Mechanics* (Springer, Berlin, 1991).
[53] R. Zwanzig, *Nonequilibrium Statistical Mechanics* (Oxford University Press, Oxford, 2001).
[54] See Supplemental Material at http://link.aps.org/supplemental/10.1103/PhysRevE.88.042406 for the derivation of Eqs. (43) and for further details on the calculation and the results in the higher temperature cases.
[55] G. Cini-Castagnoli and F. P. Ricci, J. Chem. Phys. **32**, 19 (1960).
[56] J. G. Kirkwood and F. P. Buff, J. Chem. Phys. **17**, 338 (1949).
[57] R. P. White and H. Meirovitch, Proc. Natl. Acad. Sci. USA **101**, 9235 (2004).
[58] P. Varilly and D. Chandler, J. Phys. Chem. B **117**, 1419 (2013).
[59] O. Maselli, J. R. Gascooke, W. D. Lawrance, and M. A. Buntine, J. Phys. Chem. C **113**, 637 (2009).
[60] J. F. Xie, S. S. Sazhin, and B. Y. Cao, Phys. Fluids **23**, 112104 (2011).
[61] B. Y. Cao, J. F. Xie, and S. S. Sazhin, J. Chem. Phys. **134**, 164309 (2011).
[62] A. Frezzotti, AIP Conf. Proc. **1333**, 161 (2011).
[63] D. Schanz, B. Metten, T. Kurz, and W. Lauterborn, New J. Phys. **14**, 113019 (2012).
[64] T. Ishiyama, T. Yano, and S. Fujikawa, AIP Conf. Proc. **762**, 491 (2005).
[65] W. H. Press, S. A. Teukolski, W. T. Vetterling, and B. P. Flannery, *Numerical Recipes in Fortran77: The Art of Scientific Computing*, 2nd ed. (Cambridge University Press, New York, 1992).